nature biomedical engineering

Scaled-up epidermal electrodes

ARTICLES
https://doi.org/10.1038/s41551-019-0347-x

nature biomedical engineering

Large-area MRI-compatible epidermal electronic interfaces for prosthetic control and cognitive monitoring

Limei Tian[1,2,14], Benjamin Zimmerman[2,14], Aadeel Akhtar[2,14], Ki Jun Yu[3,14], Matthew Moore[2], Jian Wu[4], Ryan J. Larsen[2], Jung Woo Lee[5], Jinghua Li[6], Yuhao Liu[6], Brian Metzger[2], Subing Qu[6], Xiaogang Guo[4], Kyle E. Mathewson[7], Jonathan A. Fan[8], Jesse Cornman[9], Michael Fatina[9], Zhaoqian Xie[10], Yinji Ma[4], Jue Zhang[6], Yihui Zhang[4], Florin Dolcos[2], Monica Fabiani[2], Gabriele Gratton[2], Timothy Bretl[11], Levi J. Hargrove[12], Paul V. Braun[6], Yonggang Huang[10] and John A. Rogers[2,6,13]*

Skin-interfaced medical devices are critically important for diagnosing disease, monitoring physiological health and establishing control interfaces with prosthetics, computer systems and wearable robotic devices. Skin-like epidermal electronic technologies can support these use cases in soft and ultrathin materials that conformally interface with the skin in a manner that is mechanically and thermally imperceptible. Nevertheless, schemes so far have limited the overall sizes of these devices to less than a few square centimetres. Here, we present materials, device structures, handling and mounting methods, and manufacturing approaches that enable epidermal electronic interfaces that are orders of magnitude larger than previously realized. As a proof-of-concept, we demonstrate devices for electrophysiological recordings that enable coverage of the full scalp and the full circumference of the forearm. Filamentary conductive architectures in open-network designs minimize radio frequency-induced eddy currents, forming the basis for structural and functional compatibility with magnetic resonance imaging. We demonstrate the use of the large-area interfaces for the multifunctional control of a transhumeral prosthesis by patients who have undergone targeted muscle-reinnervation surgery, in long-term electroencephalography, and in simultaneous electroencephalography and structural and functional magnetic resonance imaging.

Advances in soft, stretchable electronic technologies over the past decade have led to broad classes of thin, skin-interfaced medical devices, with diverse potential applications in healthcare, wellness and fitness[1–4]. These skin-like epidermal systems offer capabilities for continuous measurements of biophysical and biochemical parameters associated with physiological health and mental activity[5–9]. They can also serve as electrostimulators for neuromodulation, rehabilitation therapy and human–machine interactions[10–12]. Compared to traditional wearable devices, such systems establish robust, intimate electrical interfaces with the skin without causing irritation or discomfort, as a result of their ultrathin, low-modulus, lightweight, stretchable and breathable construction, thereby allowing for continuous, long-term monitoring in both clinical settings and at home. Although various soft electronic interfaces with skin and internal biological tissues have been developed, the sizes of these systems are typically limited to a few square centimetres, resulting in spatial mapping capabilities that extend over only small areas[1,4,13,14].

Extending the sizes of such devices to enable coverage over entire, large regions of the body is of significant interest. For instance, large-area, body-scale epidermal systems for electromyography (EMG) can provide robust recording capabilities across multiple muscle groups for accurate control of multifunction prostheses. Full-scalp or full-forehead systems for electroencephalography (EEG) can serve as monitors of electrical activity across the brain with high information content. The ability to acquire electrical recordings during functional magnetic resonance imaging (fMRI) can provide additional important capabilities for the analysis of fluctuations in physical and psychological states[15–17]. Specifically, the concurrent collection of fMRI-compatible, high-density EEG recordings with millisecond temporal resolution and three-dimensional (3D) fMRI

[1]Department of Biomedical Engineering, Texas A&M University, College Station, TX, USA. [2]Beckman Institute for Advanced Science and Technology, University of Illinois at Urbana–Champaign, Urbana, IL, USA. [3]School of Electrical and Electronic Engineering, Yonsei University, Seoul, Republic of Korea. [4]Applied Mechanics Laboratory, Department of Engineering Mechanics, Center for Mechanics and Materials and Center for Flexible Electronics Technology, Tsinghua University, Beijing, China. [5]Department of Materials Science and Engineering, Pusan National University, Busan, Republic of Korea. [6]Department of Materials Science and Engineering, Frederick Seitz Materials Research Laboratory, University of Illinois at Urbana–Champaign, Urbana, IL, USA. [7]Department of Psychology, University of Alberta, Edmonton, Alberta, Canada. [8]Department of Electrical Engineering, Stanford University, Stanford, CA, USA. [9]Department of Electrical and Computer Engineering, University of Illinois at Urbana–Champaign, Urbana, IL, USA. [10]Departments of Civil and Environmental Engineering, Mechanical Engineering, and Materials Science and Engineering, Northwestern University, Evanston, IL, USA. [11]Department of Aerospace Engineering, University of Illinois at Urbana–Champaign, Urbana, IL, USA. [12]Feinberg School of Medicine, Northwestern University, Shirley Ryan AbilityLab, Chicago, IL, USA. [13]Departments of Materials Science and Engineering, Biomedical Engineering, Neurological Surgery, Chemistry, Mechanical Engineering, Electrical Engineering and Computer Science, Simpson Querrey Institute and Feinberg Medical School Center for Bio-Integrated Electronics, Northwestern University, Evanston, IL, USA. [14]These authors contributed equally: Limei Tian, Benjamin Zimmerman, Aadeel Akhtar, Ki Jun Yu.
*e-mail: jrogers@northwestern.edu

with millimetre spatial resolution yields complementary information associated with brain activity[15,16,18].

This paper reports a class of ultra-large-area, multifunctional and MRI-compatible epidermal electrical interfaces that can reliably and robustly enable body-scale electrophysiological recordings. Our findings rest on a series of advances. First, we report materials and manufacturing approaches for large-area epidermal electrophysiological sensors to enable high-resolution electrical recordings from large regions of the body, such as the full forehead/scalp and the full circumference of the arm, at a scale 40 times larger than those of previous reports[1,4,13,14]. Second, we describe elastomeric bilayer designs and removable polymer supports that facilitate the manipulation and mounting of such large-area systems onto the curved surfaces of the body, in ways that maintain the conformal electrode–skin interface. Third, we identify microporous silicone adhesives that provide a strong, non-irritating adhesive interface to the skin with exceptional breathability. Fourth, we design filamentary electrode architectures that minimize radio frequency-induced eddy currents as the basis for fMRI compatibility.

The main content lies in: (1) materials and designs that allow scaling of epidermal electronics to areas that are orders of magnitude larger than those in previous reports[1,4,13,14], (2) quantitative theoretical and experimental investigations of the responses of these systems to radio frequency fields and magnetic field gradients found in MRI instruments, including systematic investigations of the effects of mesh topology, and (3) advanced applications in multi-nodal prosthetics control strategies that leverage the large-area systems introduced here and simultaneous MRI and EMG/EEG, enabled not only by large areas but also by mesh topologies that minimize heating and maximize MRI transparency. The use of these large-area epidermal electrical interfaces in the multifunctional control of prostheses of patients who have undergone muscle reinnervation in long-term EEG monitoring and in recording of EMG and scalp EEG during fMRI illustrates these capabilities in the context of important applications in healthcare and health science research.

Results

Materials, mechanics and manufacturing approaches. Figure 1a shows a photograph of three sets of large-area electrode arrays formed by contact-mode photolithographic processing on an eight-inch silicon wafer. Each consists of 17 fractal mesh electrodes in Greek-cross geometries, with dimensions of 1 cm × 1 cm, fill factors (the area of the metal traces divided by the area of the electrode) of 30% and total areas that can exceed 200 cm^2. Flexible cables provide interfaces to external data acquisition electronics through filamentary serpentine gold interconnect wires (110 μm width). The constituent layers of the epidermal electrical interfaces in a strip format are illustrated in Fig. 1c. The fractal mesh electrodes (Cr/Au, 5 nm/300 nm) are in direct contact with the skin; a coating of polyimide encapsulates the interconnect wires to provide electrical insulation and mechanical strain isolation. The microperforated soft silicone layer provides a highly breathable interface with the skin, with tuneable permeability properties. The micropores result from the dissolution of a monolayer assembly of poly(methyl methacrylate) microspheres (100 μm diameter), partially embedded at the near-surface region of the cross-linked adhesive silicone.

The large sizes of these systems and the designs of the soft supports represent distinguishing features compared with those of previous reports. The support consists of two layers of silicone, each with a different formulation. The layer facing away from the skin is an ultrathin, tack-free membrane (Ecoflex 00-30; 40 kPa, 8 μm thick) that weakly adheres to a film of polyethylene terephthalate (PET), thereby ensuring easy release. The second layer is a silicone adhesive (Bluestar 4642; 25 kPa, 80 μm thick) that bonds to the skin (peel adhesion of 1.2 N per 2.5 cm on the human skin, as measured with the American Society for Testing and Materials D3330 standard test method) with sufficient strength for long-duration wear. Compared with common acrylic-based adhesives used in skin bandages, the adhesion of this silicone material is much weaker but still sufficient for robust bonding due to the small interface stresses that follow from the thin, low-modulus construction of the system. This feature allows application not only to healthy skin but also to sensitive or even scarred tissue[19]. The multilayer construction provides a facile means to deliver and form robust electrical interfaces with the skin, while the removable PET sheet facilitates manual manipulation.

Figure 1c–f demonstrates the process of applying a large-area epidermal array onto the forearm, wherein the device is gently pressed onto the skin and the PET substrate is then peeled away. The earliest reports of epidermal electronics rely on the delivery of devices on water-soluble polymer sheets that subsequently dissolve[4,9]. Other approaches involve direct transfer printing from the surface of a stamp, followed by encapsulation with a spray-on bandage[7]. The scheme introduced here is substantially simpler and more reliable than these others and it scales naturally to large-area systems. Figure 1g shows the electrode arrays (17 cm × 13 cm) on a soft support covering a large region of the back of a male subject. As an additional note, the transparency of the system facilitates application onto anatomical targets, such as muscle sites of amputees, and onto locations of the scalp defined by the international 10–20 system.

As with other epidermal electronic systems, a key feature is the intimate, conformal interface with the skin, with a soft mechanical construction that avoids constraints in natural motions. Currently available flexible printed circuit board-based electronic interfaces do not offer soft, skin-like mechanical properties, which are critical for obtaining long-term, consistent, high-fidelity electrophysiological signals from the surface of the skin (Supplementary Fig. 1). Breathability is an important consideration for long-term wear. Previous reports suggest that thick silicone films (1 mm) present on the skin for several days can cause skin irritation due to trapped interfacial moisture[9]. On the other hand, thin silicone layers (65 μm) can serve as restorative synthetic skins, effectively slowing transdermal water loss from clinically dry skin with a performance that exceeds that of commercial moisturizers[20]. The bilayer soft-support design reported here allows the water vapour transmission rate to be adjusted to meet requirements without changing the chemical composition of the materials. In this way, the water-barrier properties of the soft support can be personalized to the skin or environmental conditions of the user. Specifically, in the bilayer structure, the ultrathin external facing layer allows water vapour to pass but serves to protect devices from the surrounding environment. The underlying microperforated soft silicone adhesive defines, to a significant extent, the overall breathability of the system, where the density and sizes of the pores represent the key parameters. Figure 1h,i shows a photograph and scanning electron microscope (SEM) image of a gold electrode on a microperforated silicone support, respectively. By changing the porosity, properties that range from full breathability to constrained transdermal water loss can be achieved (Fig. 1j).

Measurements show that the water vapour transmission rate (WVTR) increases with decreasing thickness of the external facing layer and increasing porosity of the silicone adhesive layer (Fig. 1j). The WVTR determined for a bilayer of a 12% microperforated silicone adhesive layer (pores with an opening diameter of 80 μm and a density of 2,000 pores cm^{-2}) and an ultrathin external facing layer (8 μm), is two times higher than that of polydimethylsiloxane (PDMS) elastomers of the same thickness, which are often used in skin-integrated electronics. The WVTR of the most breathable soft support examined is >85% of the value determined without any cover layer, shown as the open case in the results. The breathability achievable with this design is comparable to nanofilament mesh-based on-skin electronics, a highly gas-permeable system that was reported recently[9]. Finite element analysis (FEA) illustrates the

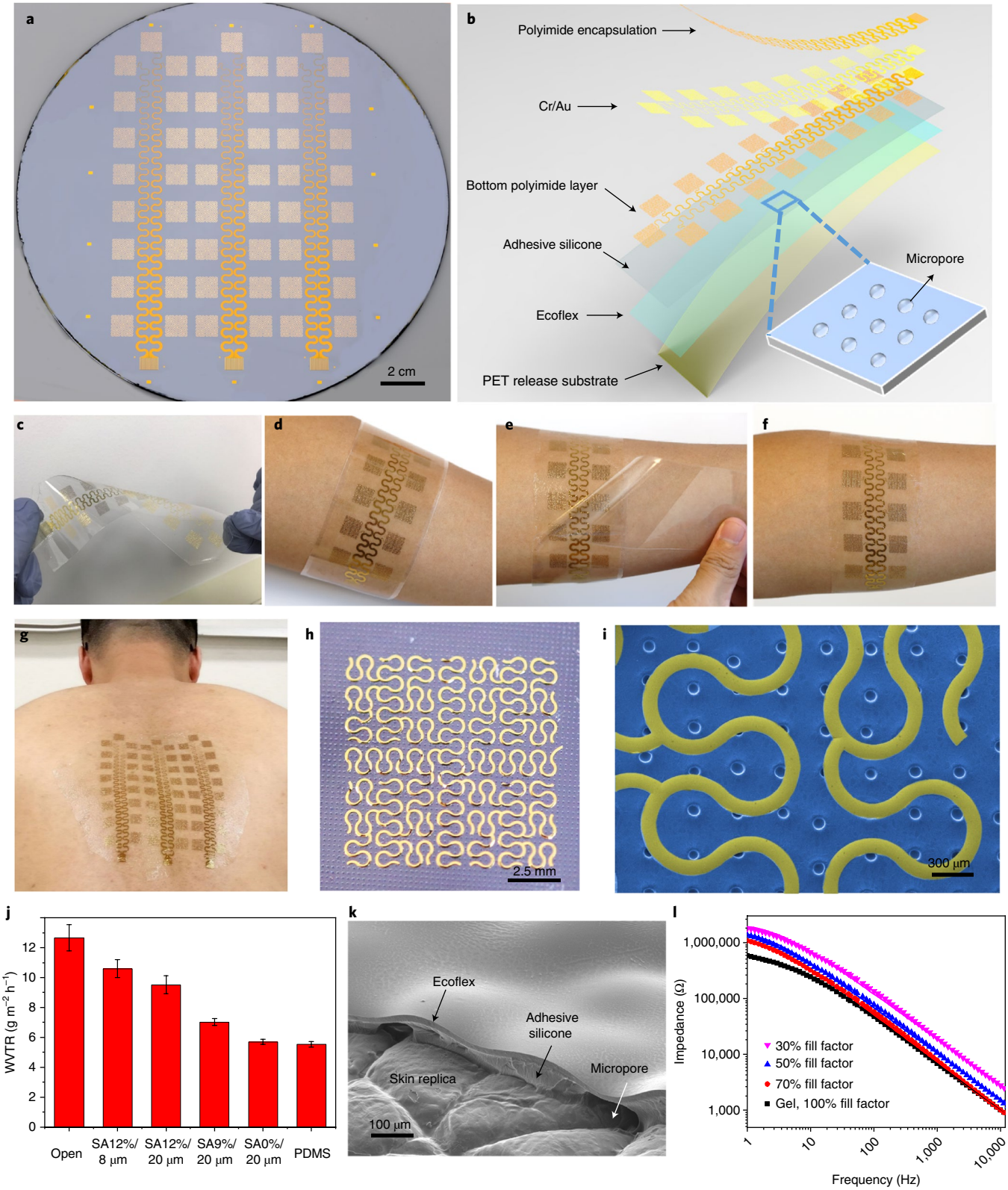

Fig. 1 | Large-area epidermal electrodes for electrophysiological mapping and prosthetic control. a, Photograph of large-area epidermal electrodes fabricated on an eight-inch silicon wafer. **b**, Exploded-view schematic illustration of the key functional layers of the flexible and stretchable devices. **c**, Photograph of a device composed of 17 electrodes on a PET release support. **d**–**f**, Photographs of the device laminated on the forearm of a subject before (**d**) and after (**e**,**f**) peeling off the PET release support. **g**, Photograph of large-area epidermal electrodes laminated on the back of a male subject. **h**, Photograph of a fractal electrode on the microperforated silicone. **i**, SEM image of gold serpentine mesh transferred on a microperforated soft silicone adhesive (SA) film. **j**, Comparison of WVTR values of different silicone adhesive films and the value without a film (open). The error bars represent the s.e.m. for three measurements. Percent values represent microperforated area percentages, μm values represent the thickness of external-facing silicone layers. **k**, SEM tilted view of a bilayer microperforated silicone support laminated on a skin replica. **l**, Electrical impedance of mesh electrodes with different fill factors (30–70%) and a soft conductive solid gel electrode (100%) measured on the skin. The individual data points represent the averages of three measurements.

mechanics of a fractal mesh electrode mounted on the bilayer elastomeric construct and laminated on the skin. The results suggest an elastic stretchability of 18% (assuming a yield strain of 0.3% for the gold), which is sufficient for strains encountered during natural motions of the skin (Supplementary Fig. 2).

The ability of electrodes to record and stimulate depends strongly on the electrical impedance of the electrode–skin interface[21,22]. As demonstrated previously, conformal contact reduces this impedance, eliminates motion artefacts and minimizes background noise[11,23]. Scanning electron microscope images of devices laminated on a silicone surface moulded into the texture of human skin (forearm) confirm the excellent conformality at the interface (Fig. 1k and Supplementary Fig. 3a–c). Measurements using electrochemical impedance spectroscopy define the contact impedance of mesh electrodes with different fill factors and a conductive solid gel electrode of the same area (1 cm × 1 cm; Fig. 1l). The gel electrode serves as a reference with a 100% fill factor to compare with the mesh electrodes with fill factors of 30, 50 and 70% (Supplementary Fig. 4). The impedance measurements span frequencies from 1 Hz to 10 kHz, which are most relevant to EEG and EMG signals. The impedance increases with decreasing fill factor due to a decrease in the effective contact area of metals with the skin. The impedance of the mesh electrode with a fill factor of 70% is only slightly higher than that of the conductive gel electrode. The impedance data can be captured quantitatively with an equivalent circuit model that consists of a resistor (R_u) in series with a parallel arrangement of a resistor (R_e) and a constant-phase element (CPE; introduced to capture the heterogeneity of the interface), as illustrated in Supplementary Fig. 5a (ref. [24]). In this treatment, the complex value (j is the imaginary unit) of the impedance as a function of angular frequency ω becomes[25]

$$Z = R_e \,/\, (1 + (j\omega)^{\alpha} Y_0 R_e) + R_u$$

where R_e represents the charge-transfer resistance of the surface of the skin, R_u represents the resistance of underlying tissue and the impedance of the CPE is $Z_{CPE} = 1 \,/\, ((j\omega)^{\alpha} Y_0)$. Specifically, Y_0 is the magnitude of $1/Z_{CPE}$ at $\omega = 1$ and α can assume a value between 0 and 1 such that the CPE acts as an ideal capacitor when $\alpha = 1$. Supplementary Fig. 5 summarizes the results of this equivalent circuit model with fitted parameters in Supplementary Table 1. The fitted R_e decreases and Y_0 increases linearly with an increasing fill factor, that is, from 30, 50 and 70 to 100% (Supplementary Fig. 5). The linear scaling trend suggests conformal contact of mesh electrodes on the skin, at a level comparable to that provided by the conductive gel. The values of R_e, $Z_{CPE|\omega=1}$ and R_u are approximately 630 kΩ, 20 MΩ and 330 Ω, respectively, indicating that the overall contact impedance is dominated by R_e.

Large-area, multichannel systems for robotic prosthesis control via EMG. The unique features of the systems summarized in Fig. 1 serve as the foundations for practical applications in human–machine interfaces, biomedical research and clinical healthcare. An example of the first application is the means for control of robotic prostheses on the basis of EMG signals generated from contractions of the muscles in a residual limb. Advanced surgical techniques, such as targeted muscle reinnervation, qualitatively expand the scope of information for this type of control. Here, the re-routing of residual nerves that carry motor information about the amputated limb to intact muscles in the residual limb increases the level of intuitive control of the prosthesis based on surface EMG[26], ideally collected with high fidelity across a large area of the residual limb.

Our system overcomes the limitations of conventional EMG interfaces, which utilize rigid, stainless-steel electrodes (~1 cm diameter, ~2 mm height) embedded in a tight-fitting, thick rubber liner (~2 mm thick; Supplementary Fig. 6a) to ensure contact between the electrodes and the skin. The resulting concentrated mechanical stresses can induce erythema, even after two hours of wear (Supplementary Fig. 6b). In addition, the motions of the electrodes relative to the skin that occur during physical activity reduce the accuracy of the control system, sometimes to an extent that requires re-training of the classifier. Sweat that accumulates at the skin interface as a result of the limited breathability of the rubber liner exacerbates this problem. In contrast, the large-area formats, thin, skin-like physical properties, low impedance skin interfaces, exceptional breathability and options in scaling to large numbers of independent electrodes associated with the systems of Fig. 1 bypass these disadvantages, thus providing an almost ideal interface for prosthetic control. The result offers a physically imperceptible system for the acquisition of stable, clinical-quality EMG signals, without slippage at the electrode–skin interface, even when located at the interface with a prosthetic socket. EMG signals can be captured reliably and consistently over several days of acquisition, during exercise (with the prosthesis on) and after sleeping and showering (without the prosthesis). Supplementary Table 3 summarizes a quantitative comparison of related parameters between conventional and epidermal electrodes.

Demonstrations of epidermal systems for this application exploit eight pairs of electrodes to provide eight channels of bipolar EMG signals. A top ground electrode enables common mode rejection (Fig. 2a). Figure 2b shows such a device deployed on a 39-year-old male subject with a right transhumeral amputation and targeted muscle-reinnervation surgery. The epidermal EMG array lies over the middle of the residual limb to achieve uniform coverage across all superficial muscle groups. The operation of the robotic prosthesis involves EMG data collection, motion classifier training and physical prosthesis control. The process starts with the amplification and band-pass filtering (85 to 300 Hz) of EMG signals collected simultaneously from all of the electrodes as the subject intuitively performed nine different motion classes: rest, elbow flexion, elbow extension, wrist supination, wrist pronation, wrist flexion, wrist extension, hand open and hand close.

Each movement elicits a different pattern of EMG signals produced by muscle activation from the residual limb (Fig. 2c). These patterns form the basis of a motion classifier via pattern recognition algorithms[26]. The resulting classifier can decode a given movement in real time on the basis of patterns of the EMG signals, for purposes of driving a transhumeral prosthesis with a powered elbow, wrist rotator and electric hand. In this manner, signals obtained with the epidermal EMG array allow the amputee to control elbow, wrist and hand movements of his prosthesis (Fig. 2d and Supplementary Video 1). The confusion matrix produced by pattern recognition algorithms shows that this type of interface provides an average classification accuracy (89%) that is slightly higher than that of conventional technologies (~84%; Supplementary Fig. 6c and Supplementary Table 2). With the current design, some crosstalk in EMG signals occurs between electrode pairs, for example, between Channels 6 and 7. Although such behaviour is typical for surface EMG recordings, the array designs could be optimized to the anatomy of patients, including electrode size, shape and spacing, to minimize such effects and further improve motion classification accuracy[27].

Following the same established experimental protocol and data analysis method, results indicated that these body-scale epidermal EMG interfaces allow for the multifunctional control of prostheses in patients who have undergone targeted muscle-reinnervation surgery. For conventional EMG systems, misalignment of the prosthesis socket, resulting in a shift in the electrode–skin contact locations, is inevitable during prosthesis donning and doffing. An electrode shift can significantly reduce the motion classification accuracy of the prosthesis and increase the trial failure rates. The electrode size, distance between electrodes, distribution of electrodes with

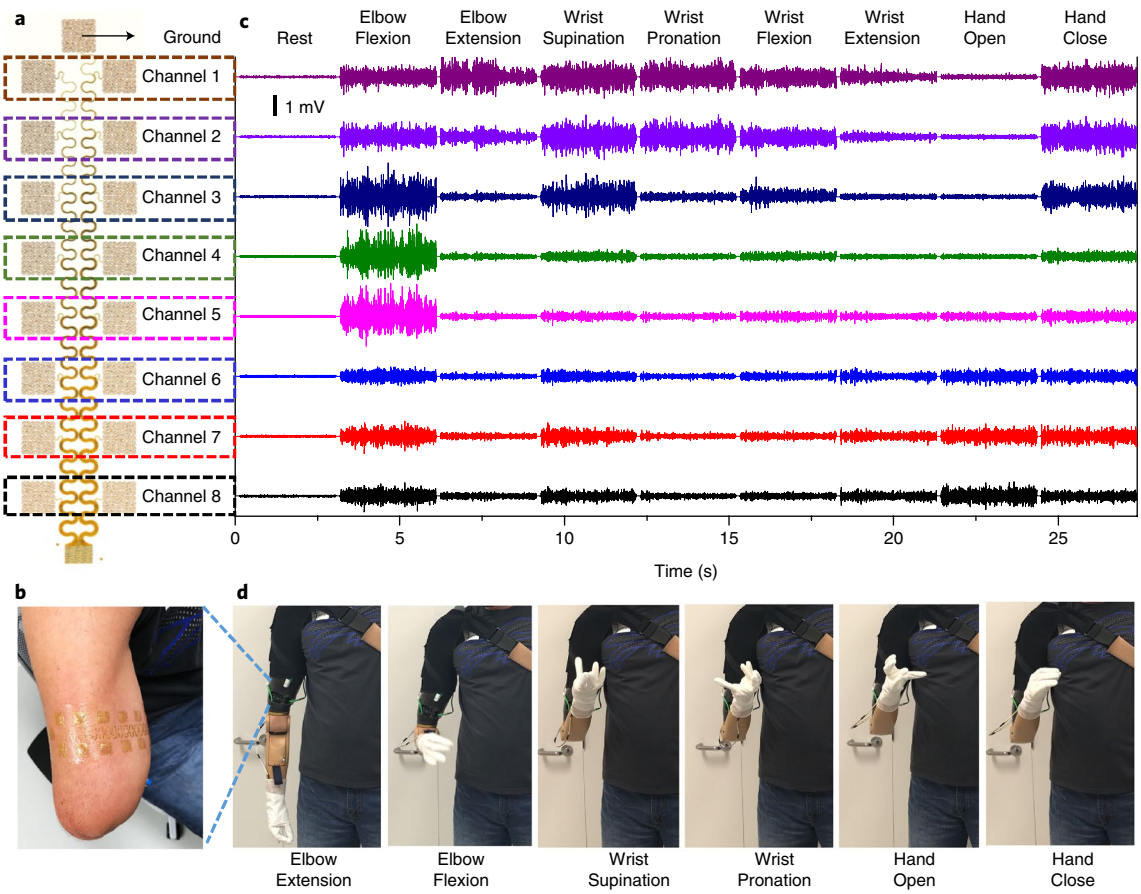

Fig. 2 | Large-area epidermal electrodes for multichannel EMG and prosthetic control. a,**b**, Photographs of a large-area EMG device on a soft support (**a**) and laminated on the amputated upper limb of a subject (**b**). **c**, Multichannel EMG values measured from the device shown in **b**. **d**, Photographs of the prosthetic movements that were intuitively performed by the subject using classified EMG signals measured from targeted reinnervated muscles in real time.

respect to muscle fibres and improved learning algorithms have previously been investigated to improve the classification robustness to electrode shift[28–31]. The epidermal interface reported here eliminates such electrode shifts, as confirmed by the similar classification accuracy after donning and doffing without re-training the classifier (Supplementary Table 4). The robust electrical interface also eliminates artefacts associated with relative motions between the electrodes and skin, as confirmed by the robustness of the motion classification despite vigorous tapping on the electrodes (Supplementary Video 2).

Such an intimate interface is also suitable for neuromuscular electrostimulation as a means to provide prosthesis control with sensory feedback[12]. Conventional rigid electrodes typically do not support conformal interfaces with the skin. For example, small air cavities can exist at the interface, thereby causing inhomogeneous distributions of injected current. Current distributions affect electrostimulation sensations, with variations that can span from comfortable touch to pain[32]. In qualitative tests with the same stimulation conditions, rigid electrodes typically lead to stinging sensations whereas epidermal electrodes provide comfortable tactile responses. Furthermore, rigid electrodes do not provide stable electrical interfaces with the skin. Variations in both the contacts and accumulation of sweat affect the electrostimulation efficiency. The associated high impedances can cause uncomfortable sensations that are not suitable for long-term sensory feedback[33,34]. Our ongoing efforts focus on utilizing these large-area interfaces to control prostheses with sensory feedback in highly dynamic conditions, including driving and sport, that require advanced pattern recognition algorithms to analyse multichannel EMG signals to eliminate stimulation artefacts.

Full-scalp multichannel systems for EEG. Full-scalp EEG is another application opportunity enabled by the large-area, conformal systems introduced here. The design of devices for this mode of use incorporates an additional layer of cross-linked conductive polyacrylate gel (100 μm; KM 30B) on top of the metal mesh electrode to further reduce the interface impedance by a factor of approximately three (at 1 Hz) via an increased fill factor from 30% (Greek-cross layout described previously) to an equivalent value that approaches 100%. This soft gel (35 kPa) results from screen-printing a precursor solution onto the electrode area (1 cm × 1 cm) and then exposing it to ultraviolet light to polymerize the material (45% glycerine, 27% potassium acrylate, 6% *N*-methyldiethanolamine, 4% triethanolamine, 4% potassium chloride, 3% fumed silica, 2% polyvinylpyrrolidone and 9% trade secret). The presence of the gel also improves the elastic stretchability of the electrodes from 18 to 26% while mounted on the skin, due to a reduction in the constraints associated with in- and out-of-plane deformations compared with those associated with the skin (Supplementary Fig. 2b). The encapsulation provided by the bilayer silicone structure, together with the comparatively non-volatile materials composition of the gel, leads to exceptionally slow drying rates, as confirmed by only a slight change in mass after exposure to open air at room temperature for two weeks, the practical limit for integration with the skin set by the timescales for exfoliation of dead cells from the stratum corneum.

The results of experiments conducted over a five-day period of continuous wear illustrate the potential for long-term EEG recording with a performance comparable to that of conventional cup EEG electrodes. Figure 3a shows two systems placed on each side of the scalp of a 28-year-old male subject. Eight electrode columns lie along the direction from the forehead to the inion on the sides of the centre line. Commercial electrodes placed down the centre line, corresponding with the 10–20 recording system locations Fz, Cz, Pz and Oz, serve as controls. Such electrodes require daily application and removal, just before and just after the time of recording, partly due to rapid drying rates of the liquid-like gel (ECI Electro-Gel). A Polhemus Fastrak electromagnetic 3D digitizer determines the locations of all of the electrodes for each measurement cycle.

The P3 event-related potential (ERP) component captured during an auditory oddball task on the first day of the five-day experiment appears in Fig. 3b for two epidermal electrodes (E1 and E2) chosen due to their proximity to the location of the Pz commercial electrode where the P3 component was largest. The P3 component recorded at Pz serves as a point of comparison. Figure 3c summarizes the ERP waveform from the average target oddball condition ($n = 181–225$ trials) minus the average standard condition ($n = 746–780$ trials) across the entire five days of the experiment, captured from electrode E1. This figure demonstrates the ability to record data across five days without removing the device or changing any normal daily activities such as showering, exercising, working and sleeping. Figure 3d highlights the consistency of the average P3 amplitude over this period with comparisons to the commercial electrode system (applied and removed daily). Figure 3e illustrates the absence of any systematic temporal variation in the signal-to-noise ratio.

The arrangement of the epidermal devices for full-scalp EEG recording appears in Fig. 3f. Here, four EEG arrays (68 electrodes) mount in a left–right direction across the scalp to demonstrate the capacity to record EEG data with full-scalp coverage. Experiments use the same auditory oddball protocol described earlier. Figure 3g shows a spatial map of the peak amplitude between 250 and 450 ms for standard and target stimuli. The signal distribution across the scalp is consistent with the expected distribution of the P3 ERP response, where peaks occur at the centro-parietal locations[35]. Figure 3h–k summarizes the average ERP for various locations on the scalp denoted in Fig. 3g, time-locked to the stimulus presentation. These plots further demonstrate the expected P3 response and distribution, with positive peaks for the targets compared with the standards over centro-parietal locations, but not in far-frontal locations and reduced elsewhere on the scalp. EEG recordings performed using a more complex task, involving emotion–cognition interactions, serve as additional demonstrations, where the results are also consistent with the literature (Supplementary Fig. 7)[36]. Careful examination of the findings in Fig. 3h–k also suggests some topography differences for the auditory N100 component (the negative-going deflection at 150 ms in the epoch). These additional components can be identified with procedures such as an independent component analysis and other advanced EEG analyses, such as source-localization, which are potentially useful in ERP research[37,38]. This collection of results confirms that high-quality EEG signals can be successfully acquired across the full scalp using large-area epidermal sensors.

Previous studies demonstrate that forehead EEGs can be used for the clinical diagnosis of status epilepticus[39], monitoring of sleep patterns[40], predicting headaches[41], and estimating vigilance and cognitive states[42]. For a full-scalp EEG, the systems reported here can be applied across the forehead, around the mastoid and on any other surface that is not covered with dense hair. In this sense, applications to newborns are promising. Conventional EEG systems rely on rigid-cup electrodes that retain liquid conductive gels and separate, bulk-wired connections, which are not suitable for long-term use due to the signal degradation that follows from drying of the gels. Epidermal interfaces offer many advantages, such as: (1) capabilities for chronic recordings (five days to two weeks) that do not interfere with normal daily activities; (2) options in high-density mapping, without the risk of electrical shorts between nearby channels; (3) the means for providing comfortable, mechanically stable interfaces that are uniquely compatible with sleep studies or sensitive/wounded skin and headgear, helmets, and so on, and (4) ease of mounting the systems, suitable for both clinical and home settings.

MRI compatibility of epidermal electrical interfaces. The MRI compatibility follows from the low electrode–skin interface impedance and the fractal layouts of the electrodes. Figure 4a illustrates the experimental setup in a 3 tesla MRI scanner. The epidermal electrodes used in the tests use a previously described design, but modified through the addition of resistors to limit current flow through the subject, as a safety precaution, to minimize heating risks due to radio frequency exposure[43]. The average electrode impedance (~30 kΩ at 30 Hz) is sufficiently low to avoid damage of the electrical recording amplifier and to ensure the high signal quality in the MRI environment. The open-mesh electrodes consisted of four units of branch-like structures, with an architecture that avoids closed loops. This design minimizes disturbance of the radio frequency magnetic field near the electrodes, thereby minimizing distortions or shadow artefacts in the magnetic resonance images.

To demonstrate these effects, we performed simulations of radio frequency fields near electrodes with various structure designs on the skin surface of a human head (Fig. 4e). In electromagnetic models, the human head is placed in the nearly uniform radio frequency field produced by a Helmholtz pair that transmits radio frequency at 128 MHz, the resonance frequency of protons at 3 tesla. Deviations from uniformity of the magnetic field are characterized by the gradient in the plane of the electrode (∇p)

$$|\nabla_p B_1| = \sqrt{\left(\frac{dB_1}{dx}\right)^2 + \left(\frac{dB_1}{dz}\right)^2}$$

where B_1 is the magnitude of the magnetic field, dB_1/dx and dB_1/dz are the two in-plane derivatives of the magnetic field, x and z are in the plane of the electrode and y is normal to the surface of the electrode on the human head (Supplementary Fig. 8a). The results demonstrate that mesh electrodes with closed designs (for example, rectangular serpentine mesh structures) induce much stronger perturbations to B_1 than those with open designs (for example, Greek-cross fractals) or those based on conventional open-ring structures (Fig. 4e). The perturbations of B_1 in the head that arise near the electrodes rapidly decrease with distance (Supplementary Fig. 8b–d). The values of $|\nabla_p B_1|$ associated with the closed-mesh electrode are more than an order of magnitude higher than that with the open design in the plane 1 mm beneath the electrode into the head (Fig. 4e). The gradient of the magnetic field along the individual coordinate axes follows the same trend (Supplementary Fig. 9). Six open-mesh electrodes with the same fill factor (30%) reveal the general effect of open electrodes on the magnetic field (Supplementary Fig. 10). The calculations show that all designs with open architectures have negligible effects on the gradient of the magnetic field, thereby suggesting minimal electrode-induced artefacts in MRI. These quantitative findings are consistent with previous qualitative observations that magnetic resonance images exhibit shadows in the vicinity of closed-, but not open-, mesh electrode designs[6].

Compared to electrophysiological signals collected outside MRI scanners, the signals collected during scans are largely impaired by artefacts associated with the MRI environment and scan sequences, including gradient, motion and cardiac-related artefacts. Standard

Fig. 3 | Large-area epidermal electrodes for multichannel EEG. a, Image of epidermal (E1 and E2) and conventional EEG cup (Pz) electrodes on the scalp of a subject. **b**, P3 ERP values recorded using epidermal and cup electrodes for comparison. **c–e**, E1 ERP values (**c**), P3 amplitude (**d**) and signal-to-noise ratio (**e**) measured with epidermal electrodes during five days of continuous wear, compared with signals collected with newly prepared cup electrodes on each day. The error bars in (**d**) represent the s.e.m. for approximately 200 trials. **f**, Photograph of 68 EEG electrodes covering the scalp of the subject. **g**, The scalp ERP map showing the potential difference between standard (left) and target (right) conditions. The ERP was averaged within the time interval of 250–450 ms. **h–k**. Representative EEG data recorded from the different areas of the scalp indicated by boxes labelled in **g**.

data-processing techniques can correct most of these artefacts to obtain levels of signal quality that compare favourably with those obtained outside of scanners. The epidermal open-mesh structures are designed to minimize the electromagnetic disturbances in the presence of MRI gradients and radio frequency pulses, thus minimizing artefacts in electrophysiological signals and radio frequency-induced heating. To demonstrate these effects, we calculated the electromagnetic fields in and around an approximate model of the head to compare those that result from the presence of conventional open-ring and epidermal open-mesh electrodes. The

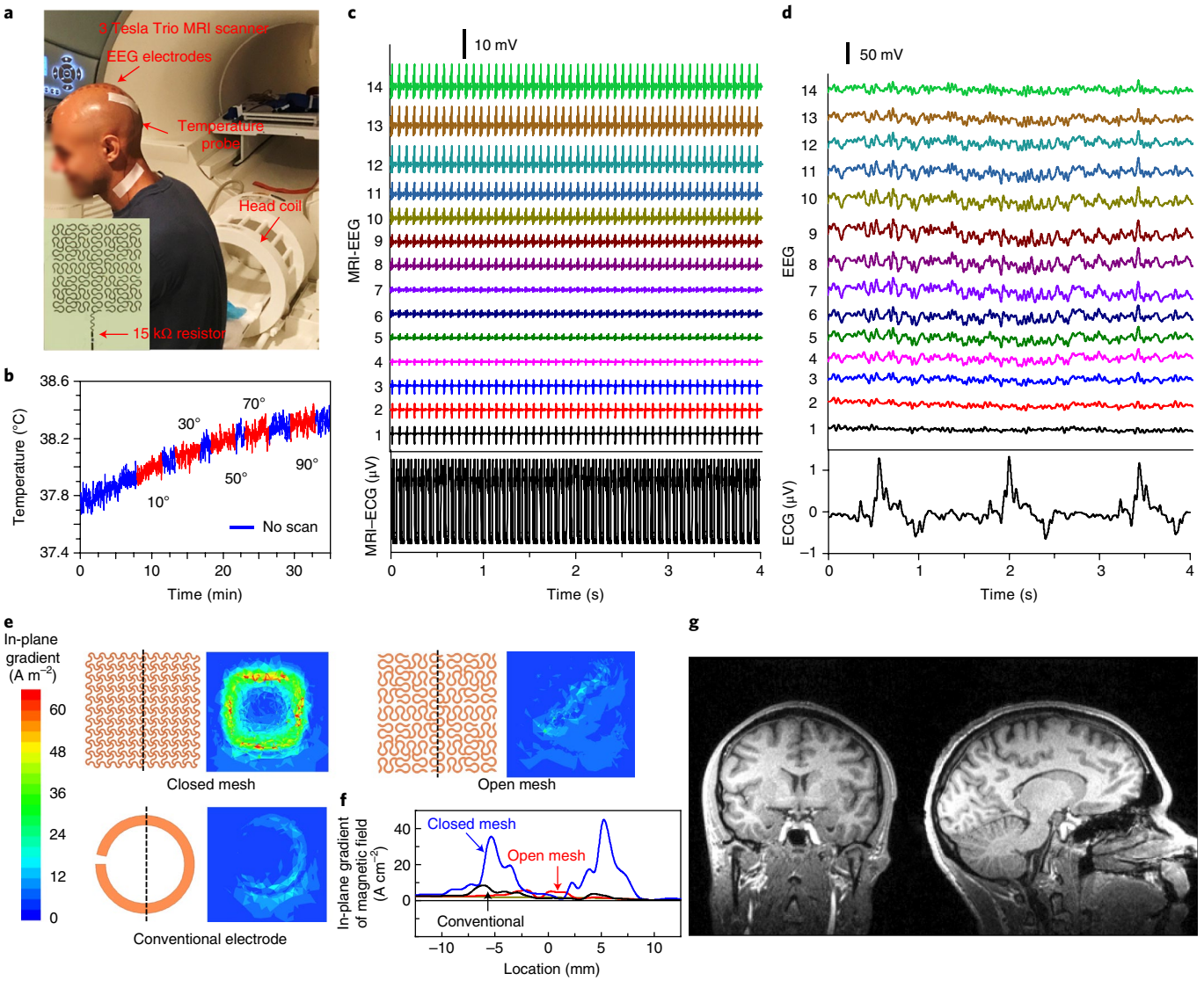

Fig. 4 | EEG/ECG performed inside an MRI scanner. a, Photograph of a subject wearing epidermal electrodes inside an MRI scanner. Inset, Photograph of an epidermal electrode with a built-in current limiting resistor. **b**, Temperature monitored under an EEG electrode at different MRI scan-flip angles and simultaneous EEG. **c**,**d**, EEG (top) and ECG (bottom) collected during MRI before (**c**) and after (**d**) the removal of magnetic resonance artefacts and low-pass filtering. Numerical labels of *y* axis represent EEG channel labels. **e**, Calculations of the in-plane gradient of the magnetic fields induced by electrodes with different structures, that is, closed-mesh, open-mesh and conventional open-ring designs. **f**, Quantitative comparison of the result for positions defined by the vertical dashed lines in **e**. **g**, Structural MRI collected during EEG recordings. The left image shows the coronal plane, and the right image shows the sagittal plane.

results show that the open-mesh and open-ring electrodes induce comparable changes in the electromagnetic fields with representative radio frequency pulses (Supplementary Fig. 11a). Under MRI gradients of 40 mT m^{-1} at 1 and 5 kHz, open-mesh electrodes induce negligible disturbances throughout the head, partly due to the small radius of curvature in the loop structure (Supplementary Fig. 11b,c). In contrast, open-ring electrodes induce much larger disturbances. These results suggest that open-mesh electrode designs might provide better options for collecting electrophysiological signals during MRI scans.

Experimental results highlight the utility of these types of epidermal open-mesh electrodes for EEG/EMG/ECG recording simultaneously with structural and functional MRI. Here, one epidermal electrode array mounts on the scalp along the centre line for EEG recordings and a single ECG electrode integrated with a 15 kΩ resistor laminates on the back, aligned with the position of the heart. During simultaneous fMRI sequences and EEG recordings at rest, a fibre-optic probe located beneath a posterior electrode on the scalp logs the temperature. The data showed only minor increases in temperature, from ~38.0 to ~38.3 °C, well below the limits set by the IEC 60601-1 standard (43 °C; Fig. 4b)[44], over an operating period of 35 min that includes five fMRI sequences with flip angles of 10, 30, 50, 70 and 90°. An important observation is that these increases in temperature are the same as those during periods without the fMRI in operation. The raw EEG and ECG data exhibit clear signatures of expected magnetic resonance gradient artefacts (Fig. 4c). Standard digital filtering techniques can remove these and they can also attenuate pulse-related artefacts. Figure 4d summarizes the ECG and EEG (after removal of ECG) following artefact subtraction. Some distortions of ECG signals result from the use of a common reference electrode for ECG and EEG located at the mastoid. The structural magnetic resonance images of the brain collected during

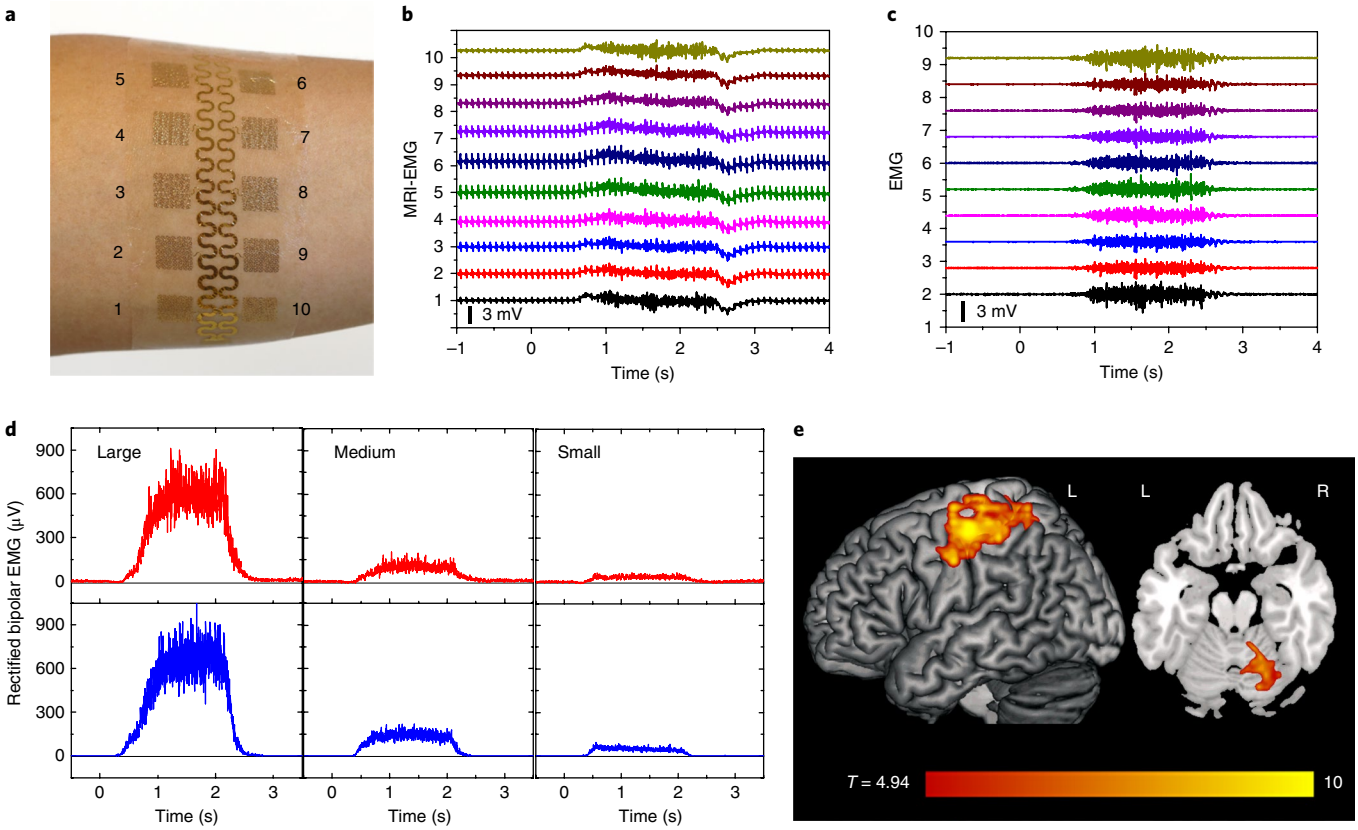

Fig. 5 | Correlation of EMG and functional MRI. a, Photograph of EMG electrodes on the right forearm of a subject located in an MRI scanner. **b**,**c**, Representative raw EMG data collected during MRI scanning from one trial (**b**) and EMG recordings after magnetic resonance artefact correction (**c**). Numerical labels in **a**, and *y* axis in **b** and **c**, represent EMG channel labels. **d**, Rectified EMG recordings from different levels of voluntary muscle contraction collected during MRI scanning (top), compared with those collected outside the MRI scanner room (bottom). **e**, Map of the association between EMG and fMRI signals overlaid on the structural MRI template, showing the pronounced association between EMG activity in the right forearm and the BOLD signal in the left motor cortex (left) and right cerebellum (right). L, left; R, right. Colour scale indicates *T*-value (the statistical value from a typical *t*-test).

electrical recordings show no distortions or shadows in the vicinity of the electrodes (Fig. 4g). The results clearly demonstrate the ability to safely record EEG and ECG signals using the epidermal electrodes in an MRI environment without degrading the quality of magnetic resonance images.

Another validation experiment involves simultaneous EMG and event-related fMRI. Here, with the epidermal EMG array on the forearm, the subject performs a muscle contraction following a visual cue inside the scanner (Fig. 5a). The visual cue instructs the subject to make a fist and to hold for 2 s during the cue presentation with different levels of muscle contraction (that is, 'Small', 'Medium' or 'Large'). Figure 5b shows representative raw data of monopolar EMG recordings from ten electrodes referenced to the top ground electrode, induced by a large degree of muscle activation. Figure 5c represents the monopolar EMG signals after removing the MRI artefacts. Rectified bipolar EMG signals result from use of ERPLAB[45]. The average rectified EMG waveforms collected from the channel pair 1–10 for each contraction level are consistent inside and outside the MRI scanner, as shown in Fig. 5d.

EMG amplitudes extracted for each trial and used for whole-brain fMRI analysis allow the relationship between EMG-measured muscle activation and fMRI-measured blood-oxygen-level dependent (BOLD) signal in the brain to be examined. The average EMG amplitude values during 1 to 2 s can be regressed onto the fMRI signals at each voxel in the brain for the time point following the onset of the trial that captures the peak of the BOLD response, on a trial-by-trial basis. The resulting statistical maps allow for the identification of associations between the muscle responses and brain activity related to the muscle contraction cues across trials (Fig. 5e). These analyses use a critical value threshold of 4.94 *t*, corresponding to $P<0.05$, family-wise error (FWE) corrected for multiple comparisons and an extent threshold of 100 voxels[46]. As expected, the results from the EMG-informed fMRI show a strong association between the EMG amplitude from the right forearm and the BOLD response, particularly in the left motor cortex ($T_{max}=11.08$; $P_{FWE}<0.05$; Montreal Neurological Institute (MNI) coordinates: $x=-32$, $y=-28$, $z=56$; $k=1{,}107$) and the right cerebellum ($T_{max}=7.23$; $P_{FWE}<0.05$; MNI coordinates: $x=20$, $y=-56$, $z=-20$; $k=141$; Fig. 5e), as well as the cuneus ($T_{max}=7.23$; $P_{FWE}<0.05$; MNI coordinates: $x=-16$, $y=-72$, $z=20$; $k=327$). These data confirm that EMG signals can be successfully acquired using the epidermal sensors in a fMRI scanning environment and that after typical data processing procedures, the EMG shows expected association with the fMRI BOLD response.

The collective results set the stage for combined EEG and EMG studies of sleep patterns, physical rehabilitation/therapy protocols and other healthcare applications that require minimally invasive measurement interfaces over large areas and data collection over periods of days or weeks. These opportunities represent topics of current work.

Outlook

The materials and device layouts reported here serve as the foundations for body-scale epidermal electronic interfaces, with important capabilities in collecting physiological information across large regions of the skin. Examples include large-area EMG devices that interface with the residual limbs of amputees with targeted muscle reinnervation to allow for the accurate control of complex multifunctional prostheses and scalp EEG systems for stable, high-fidelity operation over several days of continuous wear. The MRI compatibility of these systems, together with an underlying understanding of the key electromagnetic effects, allows the design of systems for simultaneous EEG and EMG during fMRI, which is relevant in health science research and in the monitoring of patients with epilepsy or movement disorders. Ongoing efforts focus on providing sensory feedback through electrostimulation or other means. Adapted versions of these technologies may also allow application to internal organs, including electrophysiological mapping over large areas of the brain or heart.

Methods

Device fabrication. Fabrication of large-area electrode arrays began with spin coating and curing a thin layer of polyimide (2 μm; HD Microsystems) on an oxygen plasma-treated coating of PDMS (10 μm, Dow Corning) on an eight-inch silicon wafer. Photolithography and etching of chromium (5 nm) and gold (300 nm) films deposited by electron beam evaporation yielded conductive traces with widths of 125 μm. An oxygen-plasma etch defined matching patterns in an overcoat of a 2-μm-thick layer of polyimide. A water-soluble tape (3M) allowed retrieval of the resulting structures and attachment to an adhesive silicone surface prepared in a manner described as follows. The formation of silicone bilayers involved first spin casting a layer of Ecoflex (~8 μm thick; Smooth-On) onto a thin sheet of PET (50 μm thick; Grafix DURA-LAR), followed by thermal curing and then coating the second layer of adhesive silicone (80 μm thick; RT GEL 4642, Bluestar). Transfer printing with a PDMS stamp delivered a monolayer assembly of poly(methyl methacrylate) microspheres (100 μm diameter; Cospheric LLC) onto the uncured surface of the adhesive silicone. After thermal curing, dissolving the poly(methyl methacrylate) by immersion in acetone yielded micropores in a solid adhesive silicone layer. The approach reported here simplifies the transfer of epidermal devices from rigid wafers to soft silicone supports by eliminating several fabrication steps, including Ti/SiO_2 deposition by electron beam evaporation, ultraviolet-ozone treatment of the silicone surface and chemical bonding of SiO_2-coated devices to the silicone. Previously reported strategies also require the application of water to eliminate temporary backing layers used for handling and manipulation of the devices during mounting. These collective procedures lead to reductions in reliability and challenges in scaling to large areas. The results of repetitive application of five devices with the new and the old designs reveal yields (as defined by devices mounted on the skin without defects in the form of fractures, folds or distortions) of 100% and 20%, respectively.

FEA of the mechanics. Three-dimensional FEA techniques defined the mechanical deformations and strain distributions associated with devices on human skin. Eight-node 3D solid elements modelled the skin and silicone, and four-node shell elements with a two-layer (Au/polyimide) were used for fractal electrodes, with refined meshes to ensure the computational accuracy. Displacement-type boundary conditions were assigned to the side surfaces of the human skin applied with different levels of stretching. The elastic stretchability corresponds to the point at which the maximum strain in the metal layer exceeds the yield strain (~0.3%) across at least half of the width of any section. The Young's modulus (E) and Poisson's ratio (ν) of the materials used in the simulations include $E_{Au} = 70$ GPa and $\nu_{Au} = 0.44$ for gold, and $E_{PI} = 2.5$ GPa and $\nu_{PI} = 0.27$ for polyimide. A typical hyper-elastic constitutive relation, that is, the Mooney–Rivlin law, captured the properties of the human skin ($E_{skin} = 130$ kPa and $\nu_{skin} = 0.49$), Ecoflex ($E_{Eco} = 40$ kPa and $\nu_{Eco} = 0.49$) and soft silicone adhesive ($E_{SA} = 25$ kPa and $\nu_{SA} = 0.49$) whose relevant material parameters are $C_{10} = 0.0175$ MPa, $C_{01} = 0.00436$ MPa and $D_1 = 0.923$ MPa^{-1} for the skin; $C_{10} = 0.00537$ MPa, $C_{01} = 0.00134$ MPa and $D_1 = 3$ MPa^{-1} for the Ecoflex and $C_{10} = 0.00336$ MPa, $C_{01} = 0.00084$ MPa and $D_1 = 4.8$ MPa^{-1} for the soft silicone adhesive. C_{01}, C_{10} and D_1 are the parameters of the Mooney–Rivlin model (a common model to describe the mechanical behaviour of rubber materials).

FEA simulations of the electromagnetics associated with MRI. FEA methods of the electromagnetic simulations defined the electric and magnetic fields. The head with a 92 mm radius, which includes a 8 mm-thick fat layer, 8 mm-thick bone layer and grey matter, was placed in a Helmholtz pair with a radius of 120 mm and 200 mm height. The simulations used commercial software (Ansys HFSS 15, ref. 47), where the lumped port yielded the electric and magnetic fields in the head. The in-plane gradient of the magnitude of the magnetic field underneath the electrodes (shown in Fig. 4e), was obtained from $|\nabla_p B_1| = [(dB_1/dx)^2 + (dB_1/dz)^2]^{1/2}$ with a working frequency of 128 MHz.

EMG recording for prosthesis control. One male with a right transhumeral amputation (age 39 years) participated in the experiment. After using an alcohol wipe to prepare the skin, the epidermal EMG array was placed over the middle of the residual limb to achieve uniform coverage over all of the superficial muscle groups in the residual limb. The subject followed instructions displayed on a computer screen and performed nine movements in a random order with a consistent and comfortable level of effort. The movements included rest, elbow flexion, elbow extension, wrist supination, wrist pronation, wrist flexion, wrist extension, hand open and hand close. The EMG signals simultaneously collected from all of the electrodes (sampling rate, 1 kHz) were amplified using a TI ADS1299 biopotential amplifier and analogue–digital converter (Texas Instruments) and band-pass filtered from 85 to 300 Hz in real time using a TI OMAP processor (Texas Instruments). EMG signals were collected in eight consecutive trials. In each trial, the subject performed each motion twice with 4 s of hold time. The interval time between each motion was 3 s in all of the trials. The first four trials of EMG signals defined the motion classifier and the other four trials tested the classification accuracy. The pattern recognition algorithm used linear discriminant analysis to determine the motion classes sent to the prosthesis[11,26]. A motion classification was made every 25 ms using a 200 ms sliding window. Following each motion classification, a command was sent to the prosthesis to control the corresponding action. The prosthesis is a combination of an arm for elbow and wrist components (Rehabilitation Institute of Chicago)[48], and an OttoBock transcarpal hand (OttoBock), powered by a lithium polymer battery. The experimental protocol was approved by the Institutional Review Board of the University of Illinois (IRB no. 13920) and the participant gave informed consent.

Scalp EEG recording of auditory oddball task. One healthy male subject (age 28 years) participated in the scalp EEG recordings. These recordings consisted of two experiments: a multi-day experiment with five recording sessions and a separate recording session with expanded scalp coverage. The participant underwent recording of EEG data while performing an auditory oddball task presented using the PsychToolbox for Matlab. During the task, the participant detected oddball target stimuli (1,500 Hz frequency tones) presented within a string of standard stimuli (1,000 Hz frequency tones). The stimuli were presented for 16 ms (with a 2 ms ramp up and 2 ms ramp down) with a randomly jittered interstimulus interval between 500 and 1,000 ms. The infrequent target stimuli were presented at a proportion of ~20%, determined by probability on a single trial basis. The task was split into two blocks of 500 trials. In the first block, the participant was instructed to tap his left hand for targets and his right hand for standards. In the second block, the participant was instructed to tap his right hand for targets and his left hand for standards. All target trials and standard trials were collapsed across blocks to yield a 1,000 trial dataset for each recording session. The experimental protocol was approved by the Institutional Review Board of the University of Illinois (IRB no. 17075) and the participant gave informed consent.

EEG data acquisition, preprocessing and analysis. The 5 d experiment involved 43 electrodes in total, including two devices with 16 electrodes each, and 11 commercial Ag/AgCl cup electrodes. Four of the commercial electrodes were placed down the centre line of the scalp at Fz, Cz, Pz and Oz using the standard positions described by the 10–20 International System. Two served as mastoid references, one served as a ground, on the forehead, and the remaining four were located at the outer canthi of the left and right eyes and above and below the right eye to detect horizontal and vertical electrooculography (EOG).

On each day, the subject performed an auditory oddball task, involving 1,000 trials, each acquired at a sampling rate of 500 Hz using two separate amplifiers (BrainAmp, Brain Products) and an online band-pass filter between 0.1 and 250 Hz. Data were processed using EEGLAB[49], downsampled to 250 Hz, filtered with a low-pass finite impulse response (FIR) filter at 30 Hz, high-pass FIR filtered at 0.1 Hz and re-referenced to an average mastoid reference. This acquisition and preprocessing was repeated for five consecutive days without removing the epidermal devices. Commercial electrodes were applied and removed before and after performing the task on each day. The application of electrodes on the skin involved abrading the skin and applying conductive gel. Seven of 32 channels exhibited impedances over 100 kΩ on the fifth day of recording due to hair growth and were excluded from the analysis. All trials in which EEG data exceeded ±70 μV in amplitude were rejected, to remove trials likely to be affected by eye movements or blinks. The average P3 ERPs were computed time-locked to the onset of the stimulus presentation subtracting the average of data collected in the 200 ms before the stimulus presentation as baseline.

A second, single-day experiment was conducted with expanded scalp coverage. Four 17-channel epidermal arrays were used, providing the capability for full scalp EEG recording through 68 potential electrode locations. Some of these electrodes were eliminated to create space for EOG recording electrodes and reference electrodes. The experiments involved a total of 66 electrodes (the maximum that can be accommodated with two BrainAmp amplifiers): 60 array recording

electrodes, three single epidermal electrodes placed at the outer canthi of the left and right eyes and below the right eye to record EOG, two single epidermal reference electrodes placed at the mastoids and one of the array electrodes used as a ground on the right side of the head. Five-hundred trials from the auditory oddball task described previously were conducted for the full-scalp EEG experiment. All recording and analysis parameters were the same as those used in the five-day experiment.

Simultaneous EEG, ECG, and MRI acquisition, preprocessing and analysis. MRI scanning used a 3 tesla Siemens MAGNETOM Trio system equipped with an eight-channel head array transmit/receive coil (RAPID MR International). High-resolution structural information was obtained with a magnetization prepared rapid gradient echo structural scan; field of view (FOV): 230 mm × 230 mm, 256 × 256 matrix size, 0.9 mm slice thickness, 192 slices, repetition time = 2,000 ms, echo time = 2.32 ms, inversion time = 900 ms and generalized autocalibrating partial parallel acquisition (GRAPPA) acceleration factor 2. Functional MRI data were collected with an echo-planar imaging scan; FOV: 240 mm × 240 mm, 92 × 92 matrix size, 4 mm slice thickness with 10% distant factor, 25 slices, repetition time = 2,000 ms, echo time = 25 ms and GRAPPA acceleration factor 2. We performed five scans, each consisting of 100 measurements and flip angles of 10, 30, 50, 70 and 90°.

EEG data were acquired from an epidermal electrode array on the head. ECG data were acquired from an epidermal electrode placed on the back of the participant, near the heart. A 15 kΩ resistor was integrated near the electrode to minimize radio frequency-induced currents. The electrodes were connected to an MRI-compatible amplifier (Brain Products BrainAmp MR Plus) via anisotropic conductive film. Data were sampled at a rate of 5,000 Hz and processed using a Brain Vision Analyzer 2 (Brain Products) for the removal of magnetic resonance gradient and pulse artefacts, followed by exporting to EEGLAB[49] for segmenting and low-pass FIR filtering at 30 Hz.

Simultaneous EMG and fMRI acquisition, preprocessing and analysis. MRI scanning used a 3 tesla Siemens MAGNETOM Trio system equipped with an eight-channel head array transmit/receive coil. High-resolution structural information was obtained with a magnetization prepared rapid gradient echo structural scan; FOV: 230 mm × 230 mm, 256 × 256 matrix size, 0.9 mm slice thickness, 192 slices, repetition time = 2,000 ms, echo time = 2.32 ms, inversion time = 900 ms and GRAPPA acceleration factor 2. Functional MRI data were collected with an echo-planar imaging scan; FOV: 240 mm × 240 mm, 92 × 92 matrix size, 4 mm slice thickness with 10% distant factor, 25 slices, repetition time = 2,000 ms, echo time = 30 ms, GRAPPA acceleration factor 2 and 90° flip angle.

Preprocessing of fMRI data was performed using SPM12 (Wellcome Department of Cognitive Neurology), and analyses were performed using SPM12 and in-house MATLAB tools[50,51]. For preprocessing, fMRI data were first corrected for differences in acquisition time between slices for each image. Second, each functional image was spatially realigned to the first image of each run to correct for head movement and was co-registered to the high-resolution 3D anatomical image of the participant. Third, these functional images were transformed into the standard anatomical space defined by the MNI template implemented in SPM12. Finally, the normalized functional images were spatially smoothed using an 8 mm Gaussian kernel, full-width-at-half-maximum, to increase the signal-to-noise ratio. For analyses, in-house custom MATLAB scripts involving whole-brain voxel-wise analyses were used to identify the repetition time or time point following trial onset where the peak of BOLD response occurred in expected brain regions such as the motor cortex[35,37]. This examination was performed by selectively averaging the normalized smoothed functional brain images as a function of trial type (that is, Small, Medium and Large) and time point (one pre-stimulus and five post-stimulus onset time points). No assumption was made about the shape of the haemodynamic response function because this method allows finer comparisons of the magnetic resonance signal on a repetition time-by-repetition time basis. The analysis produced whole-brain average maps for each condition and repetition time or time point, which identified the time point covering 6–8 s post-stimulus onset as the clearest peak of BOLD response in regions such as the motor cortex for each condition. Thus, to identify coupling between variations in brain response and muscle contractions, fMRI-EMG associations were examined between the fMRI signals at this time point and EMG amplitude, on a trial-by-trial basis.

EMG data were acquired using an epidermal electrode array placed on the right forearm and a Brain Products BrainAmp MR Plus, at a sampling rate of 5,000 Hz. The participant underwent recording of fMRI and EMG while performing a muscle contraction task. A visual cue instructed the participant to make a fist and to hold for the 2 s duration of the cue presentation, using different levels of muscle contraction (that is, Small, Medium or Large). The experiment consisted of five blocks of 18 trials each, for a total of 90 muscle contractions. Each contraction level was cued six times per block in a counterbalanced order, providing a total of 30 trials per contraction level. As noted above, the contraction cues were presented for 2 s and were followed by the presentation of a fixation cross for 20 s during each interstimulus interval. For the purposes of analyses, all muscle contraction trials were used to examine the coupling between EMG and fMRI BOLD signals. Data were processed using Brain Vision Analyzer 2 (Brain Products) for magnetic resonance gradient artefact removal, followed by exporting to EEGLAB[49] for down-sampling to 500 Hz and high-pass FIR filtering at 10 Hz. Bipolar channel pairs were calculated and rectified using ERPLAB[45]. EMG data were then segmented time-locked to the onset of the stimulus cue, using a time window of −1,000 to 4,000 ms. Finally, the average waveforms for each condition were reported.

Reporting Summary. Further information on research design is available in the Nature Research Reporting Summary linked to this article.

Code availability

EEGLAB is freely available (http://www.sccn.ucsd.edu/eeglab/) under the GNU public license for non-commercial use and open source development, together with sample data, a user's tutorial and extensive documentation. In-house MATLAB tools were adapted from the software tools developed at Duke University (https://wiki.biac.duke.edu/biac:tools) and are available on request.

Data availability

The authors declare that all data supporting the findings of this study are available within the paper and its Supplementary Information.

Received: 2 July 2018; Accepted: 2 January 2019;
Published online: 18 February 2019

References

1. Heikenfeld, J. et al. Wearable sensors: modalities, challenges, and prospects. *Lab Chip* **18**, 217–248 (2018).
2. Rogers, J. A., Someya, T. & Huang, Y. Materials and mechanics for stretchable electronics. *Science* **327**, 1603–1607 (2010).
3. Liu, Y., Pharr, M. & Salvatore, G. A. Lab-on-Skin: a review of flexible and stretchable electronics for wearable health monitoring. *ACS Nano* **11**, 9614–9635 (2017).
4. Kim, D.-H. et al. Epidermal electronics. *Science* **333**, 838–843 (2011).
5. Tian, L. et al. Flexible and stretchable 3ω sensors for thermal characterization of human skin. *Adv. Funct. Mater.* **27**, 1701282 (2017).
6. Fan, J. A. et al. Fractal design concepts for stretchable electronics. *Nat. Commun.* **5**, 3266 (2014).
7. Yeo, W.-H. et al. Multifunctional epidermal electronics printed directly onto the skin. *Adv. Mater.* **25**, 2773–2778 (2013).
8. Webb, R. C. et al. Ultrathin conformal devices for precise and continuous thermal characterization of human skin. *Nat. Mater.* **12**, 938–944 (2013).
9. Miyamoto, A. et al. Inflammation-free, gas-permeable, lightweight, stretchable on-skin electronics with nanomeshes. *Nat. Nanotechnol.* **12**, 907–913 (2017).
10. Norton, J. J. S. et al. Soft, curved electrode systems capable of integration on the auricle as a persistent brain-computer interface. *Proc. Natl Acad. Sci. USA* **112**, 3920–3925 (2015).
11. Jeong, J. W. et al. Materials and optimized designs for human-machine interfaces via epidermal electronics. *Adv. Mater.* **25**, 6839–6846 (2013).
12. Xu, B. X. et al. An epidermal stimulation and sensing platform for sensorimotor prosthetic control, management of lower back exertion, and electrical muscle activation. *Adv. Mater.* **28**, 4462–4471 (2016).
13. Won, S. M. et al. Recent advances in materials, devices, and systems for neural interfaces. *Adv. Mater.* **30**, 1800534 (2018).
14. Minev, I. R. et al. Electronic dura mater for long-term multimodal neural interfaces. *Science* **347**, 159–163 (2015).
15. Ullsperger, M. & Debener, S. (eds) *Simultaneous EEG and fMRI: Recording, Analysis, and Application.* (New York, Oxford University Press, 2010).
16. Ritter, P. & Villringer, A. Simultaneous EEG–fMRI. *Neurosc. Biobehav. Rev.* **30**, 823–838 (2006).
17. MacIntosh, B. et al. Improving functional magnetic resonance imaging motor studies through simultaneous electromyography recordings. *Hum. Brain Mapp.* **28**, 835–845 (2007).
18. Neuner, I., Arrubla, J., Felder, J. & Shah, N. J. Simultaneous EEG–fMRI acquisition at low, high and ultra-high magnetic fields up to 9.4 T: perspectives and challenges. *Neuroimage* **102**, 71–79 (2014).
19. Matsumura, H. et al. Removal of adhesive wound dressing and its effects on the stratum corneum of the skin: comparison of eight different adhesive wound dressings. *Int. Wound. J.* **11**, 50–54 (2014).
20. Lee, J. W. et al. Soft, thin skin-mounted power management systems and their use in wireless thermography. *Proc. Natl Acad. Sci. USA* **113**, 6131–6136 (2016).
21. McAdams, E. T., Jossinet, J., Lackermeier, A. & Risacher, F. Factors affecting electrode–gel–skin interface impedance in electrical impedance tomography. *Med. Biol. Eng. Comput.* **34**, 397–408 (1996).
22. Chi, Y. M., Jung, T. P. & Cauwenberghs, G. Dry-contact and noncontact biopotential electrodes: methodological review. *IEEE Rev. Biomed. Eng.* **3**, 106–119 (2010).

23. Lee, S. M. et al. Self-adhesive epidermal carbon nanotube electronics for tether-free long-term continuous recording of biosignals. *Sci. Rep.* **4**, (2014).
24. Kontturi, K., Murtomaki, L., Hirvonen, J., Paronen, P. & Urtti, A. Electrochemical characterization of human skin by impedance spectroscopy: the effect of penetration enhancers. *Pharm. Res.* **10**, 381–385 (1993).
25. Kalia, Y. N. & Guy, R. H. The electrical characteristics of human skin in vivo. *Pharm. Res.* **12**, 1605–1613 (1995).
26. Kuiken, T. A. et al. Targeted muscle reinnervation for real-time myoelectric control of multifunction artificial arms. *JAMA* **301**, 619–628 (2009).
27. Chowdhury, R. H. et al. Surface electromyography signal processing and classification techniques. *Sensors* **13**, 12431–12466 (2013).
28. Young, A. J., Hargrove, L. J. & Kuiken, T. A. The effects of electrode size and orientation on the sensitivity of myoelectric pattern recognition systems to electrode shift. *IEEE Trans. Biomed. Eng.* **58**, 2537–2544 (2011).
29. Pan, L., Zhang, D., Jiang, N., Sheng, X. & Zhu, X. Improving robustness against electrode shift of high density EMG for myoelectric control through common spatial patterns. *J. Neuroeng. Rehabil.* **12**, 110 (2015).
30. Young, A. J., Hargrove, L. J. & Kuiken, T. A. Improving myoelectric pattern recognition robustness to electrode shift by changing interelectrode distance and electrode configuration. *IEEE Trans. Biomed. Eng.* **59**, 645–652 (2012).
31. Li, Q. X. et al. Improving robustness against electrode shift of sEMG based hand gesture recognition using online semi-supervised learning. *2016 International Conference on Machine Learning and Cybernetics. IEEE*, **1**, 344–349 (2016).
32. Keller, T. & Kuhn, A. Skin properties and the influence on electrode design for transcutaneous (surface) electrical stimulation. *2009 World Congress on Medical Physics and Biomedical Engineering.* 492–495 (Springer, Heidelberg, 2009).
33. Kaczmarek, K. A., Webster, J. G., Bachyrita, P. & Tompkins, W. J. Electrotactile and vibrotactile displays for sensory substitution systems. *IEEE Trans. Biomed. Eng.* **38**, 1–16 (1991).
34. Akhtar, A., Sombeck, J., Boyce, B. & Bretl, T. Controlling sensation intensity for electrotactile stimulation in human-machine interfaces. *Sci. Robot.* **3**, 9770 (2018).
35. Ji, J., Porjesz, B., Begleiter, H. & Chorlian, D. P300: the similarities and differences in the scalp distribution of visual and auditory modality. *Brain Topogr.* **11**, 315–327 (1999).
36. Singhal, A. et al. Electrophysiological correlates of fearful and sad distraction on target processing in adolescents with attention deficit-hyperactivity symptoms and affective disorders. *Front. Integr. Neurosci.* **6**, 119 (2012).
37. Murray, M. M., Brunet, D. & Michel, C. M. Topographic ERP analyses: a step-by-step tutorial review. *Brain Topogr.* **20**, 249–264 (2008).
38. Murray, M. M., De Lucia, M., Brunet, D. & Michel, C. M. in *Brain Signal Analysis: Advances in Neuroelectric and Neuromagnetic Methods* (ed. Handy, T. C.) 21–53 (MIT Press, Cambridge, 2009).
39. Muraja-Murro, A. et al. Forehead EEG electrode set versus full-head scalp EEG in 100 patients with altered mental state. *Epilepsy Behav.* **49**, 245–249 (2015).
40. Huang, C.-S. et al. Knowledge-based identification of sleep stages based on two forehead electroencephalogram channels. *Front. Neurosci.* **8**, 263 (2014).
41. Lin, C. T. et al. Forehead EEG in support of future feasible personal healthcare solutions: sleep management, headache prevention, and depression treatment. *IEEE Access* **5**, 10612–10621 (2017).
42. Wei-Long, Z. & Bao-Liang, L. A multimodal approach to estimating vigilance using EEG and forehead EOG. *J. Neural Eng.* **14**, 026017 (2017).
43. Lemieux, L., Allen, P. J., Franconi, F., Symms, M. R. & Fish, D. R. Recording of EEG during fMRI experiments: patient safety. *Magn. Reson. Med.* **38**, 943–952 (1997).
44. Kuusela, L., Turunen, S., Valanne, L. & Sipilä, O. Safety in simultaneous EEG-fMRI at 3 T: temperature measurements. *Acta Radiol.* **56**, 739–745 (2015).
45. Lopez-Calderon, J. & Luck, S. J. ERPLAB: an open-source toolbox for the analysis of event related potentials. *Front. Hum. Neurosci.* **8**, 213 (2014).
46. Taylor, R. Interpretation of the correlation coefficient: a basic review. *J. Diagn. Med. Sonog.* **6**, 35–39 (1990).
47. *Ansys HFSS User's Guide* (Ansys Inc., 2012).
48. Lenzi, T., Lipsey, J. & Sensinger, J. W. The RIC Arm—a small anthropomorphic transhumeral prosthesis. *IEEE ASME Trans. Mechatron.* **21**, 2660–2671 (2016).
49. Delorme, A. & Makeig, S. EEGLAB: an open source toolbox for analysis of single-trial EEG dynamics including independent component analysis. *J. Neurosci. Methods* **134**, 9–21 (2004).
50. Dolcos, F. & McCarthy, G. Brain systems mediating cognitive interference by emotional distraction. *J. Neurosci.* **26**, 2072–2079 (2006).
51. Iordan, A. D. & Dolcos, F. Brain activity and network interactions linked to valence-related differences in the impact of emotional distraction. *Cereb. Cortex* **27**, 731–749 (2017).

Acknowledgements

Device fabrication and development were carried out in part in the Frederick Seitz Materials Research Laboratory Central Research Facilities and Micro-Nano-Mechanical Systems Cleanroom, University of Illinois. L.T. acknowledges the support from Beckman Institute Postdoctoral Fellowship at UIUC. The materials and device engineering aspects of the research were supported by the Center for Bio-Integrated Electronics at Northwestern University. MRI experiments were performed at the Biomedical Imaging Center at the Beckman Institute, which also provided pilot hour support. K.J.Y. acknowledges the support from the National Research Foundation of Korea (grant nos NRF-2017R1C1B5017728 and NRF-2018M3A7B4071109) and the Yonsei University Future-leading Research Initiative (grant nos RMS2 2018-22-0028). Z.X. acknowledges the support from National Natural Science Foundation of China (grant no. 11402134). Y.H. acknowledges the support from NSF (grant nos 1400169, 1534120 and 1635443). J.W.L. gratefully acknowledges support from National Research Foundation of Korea (grant nos NRF-2017M3A7B4049466 and NRF-2018R1C1B5045721). M.M. acknowledges the support provided by Beckman Institute Predoctoral and Postdoctoral Fellowships. F.D. acknowledges the support provided by a Helen Corley Petit Scholarship in Liberal Arts and Sciences and an Emanuel Donchin Professorial Scholarship in Psychology from the University of Illinois. The authors would like to thank F. Lam for valuable discussions on electromagnetic simulations. We thank representatives of BrainVision LLC and Easycap GmbH for helpful conversations related to the equipment adaptations required for this project.

Author contributions

L.T., B.Z., A.A., K.J.Y. and J.A.R. designed the project. L.T., B.Z., B.M., K.E.M, M.F. and G.G. conceived and performed long-term EEG studies. L.T., A.A., J.C., M.F., T.B. and L.J.H. conceived and performed EMG experiments on patients for prosthesis control. L.T., B.Z., M.M., R.J.L., J.A.F. and F.D. performed simultaneous electrophysiological recordings and MRI. J.W.L., J.L., Y.L., S.Q., J.Z. and P.V.B. assisted in the fabrication of devices and materials characterization. X.G., J.W., Z.X., Y.M., Y.Z. and Y.H. performed the mechanical and electromagnetic simulations. L.T., B.Z., A.A., M.M. and J.A.R. wrote the manuscript and K.E.M, R.J.L., J.A.F. J.W., Y.H. and F.D. provided feedback on the manuscript.

Competing interests

The authors declare no competing interests

Additional information

Supplementary information is available for this paper at https://doi.org/10.1038/s41551-019-0347-x.

Reprints and permissions information is available at www.nature.com/reprints.

Correspondence and requests for materials should be addressed to J.A.R.

Publisher's note: Springer Nature remains neutral with regard to jurisdictional claims in published maps and institutional affiliations.

© The Author(s), under exclusive licence to Springer Nature Limited 2019

nature research

Corresponding author(s): John A. Rogers

Reporting Summary

Nature Research wishes to improve the reproducibility of the work that we publish. This form provides structure for consistency and transparency in reporting. For further information on Nature Research policies, see Authors & Referees and the Editorial Policy Checklist.

Statistical parameters

When statistical analyses are reported, confirm that the following items are present in the relevant location (e.g. figure legend, table legend, main text, or Methods section).

n/a	Confirmed	
☐	☒	The exact sample size (*n*) for each experimental group/condition, given as a discrete number and unit of measurement
☐	☒	An indication of whether measurements were taken from distinct samples or whether the same sample was measured repeatedly
☒	☐	The statistical test(s) used AND whether they are one- or two-sided *Only common tests should be described solely by name; describe more complex techniques in the Methods section.*
☐	☒	A description of all covariates tested
☐	☒	A description of any assumptions or corrections, such as tests of normality and adjustment for multiple comparisons
☐	☒	A full description of the statistics including central tendency (e.g. means) or other basic estimates (e.g. regression coefficient) AND variation (e.g. standard deviation) or associated estimates of uncertainty (e.g. confidence intervals)
☐	☒	For null hypothesis testing, the test statistic (e.g. *F*, *t*, *r*) with confidence intervals, effect sizes, degrees of freedom and *P* value noted *Give P values as exact values whenever suitable.*
☒	☐	For Bayesian analysis, information on the choice of priors and Markov chain Monte Carlo settings
☒	☐	For hierarchical and complex designs, identification of the appropriate level for tests and full reporting of outcomes
☒	☐	Estimates of effect sizes (e.g. Cohen's *d*, Pearson's *r*), indicating how they were calculated
☐	☒	Clearly defined error bars *State explicitly what error bars represent (e.g. SD, SE, CI)*

Our web collection on statistics for biologists may be useful.

Software and code

Policy information about availability of computer code

Data collection	Control Algorithms for Prosthetics System (CAPS) (Rehabilitation Institute of Chicago, Chicago, Illinois) for EMG recordings in prosthetic control. BrianVision recorder (Brain products) for electrical recordings in an MRI environment. A 3 Tesla Siemens MAGNETOM Trio system equipped with an 8-channel head array transmit/receive coil (RAPID MR International, Columbus, Ohio) for MRI scanning. MPRAGE (Magnetization Prepared RApid Gradient Echo) scan for structural MRI collection, and Echo-Planar Imaging (EPI) scan for functional MRI collection.
Data analysis	Control Algorithms for Prosthetics System (CAPS) (Rehabilitation Institute of Chicago, Chicago, Illinois) for EMG analysis in prosthetic control. Brain Vision Analyzer 2 (Brain Products) for MR gradient artifact and pulse artifact removal; EEGLAB for segmenting and low-pass FIR filtering at 30 Hz. SPM12 (Wellcome Department of Cognitive Neurology, London, UK) and in-house MATLAB tools for fMRI data analysis. In-house MATLAB tools are adapted from the software tools developed at Duke University (https://wiki.biac.duke.edu/biac:tools).

For manuscripts utilizing custom algorithms or software that are central to the research but not yet described in published literature, software must be made available to editors/reviewers upon request. We strongly encourage code deposition in a community repository (e.g. GitHub). See the Nature Research guidelines for submitting code & software for further information.

Data

Policy information about availability of data

All manuscripts must include a data availability statement. This statement should provide the following information, where applicable:

- Accession codes, unique identifiers, or web links for publicly available datasets
- A list of figures that have associated raw data
- A description of any restrictions on data availability

The authors declare that all data supporting the findings of this study are available within the paper and its Supplementary Information.

Field-specific reporting

Please select the best fit for your research. If you are not sure, read the appropriate sections before making your selection.

☒ Life sciences ☐ Behavioural & social sciences ☐ Ecological, evolutionary & environmental sciences

For a reference copy of the document with all sections, see nature.com/authors/policies/ReportingSummary-flat.pdf

Life sciences study design

All studies must disclose on these points even when the disclosure is negative.

Sample size	No sample size calculation was performed. Sample size of 20 provide sufficient information on different types of electrical recordings and repeatability.
Data exclusions	All trials in which EEG data exceeded ±70 µV in amplitude were rejected, to remove trials likely affected by eye movements or blinks (as stated in Methods).
Replication	EMG recordings for prosthesis control were repeated more than five times. Five-day EEG experiments were repeated twice. The results were replicable.
Randomization	All devices tested were selected randomly.
Blinding	The investigators were blinded to to group allocation during data collection and analysis.

Reporting for specific materials, systems and methods

Materials & experimental systems

n/a	Involved in the study
☒	☐ Unique biological materials
☒	☐ Antibodies
☒	☐ Eukaryotic cell lines
☒	☐ Palaeontology
☒	☐ Animals and other organisms
☐	☒ Human research participants

Methods

n/a	Involved in the study
☒	☐ ChIP-seq
☒	☐ Flow cytometry
☐	☒ MRI-based neuroimaging

Human research participants

Policy information about studies involving human research participants

Population characteristics	Participants in the EEG experiments were healthy subjects. Participants in the EMG/prosthesis control experiments were patients who had undergone targeted muscle-reinnervation surgery.
Recruitment	The participant in the EEG/MRI experiments is one of the investigators, who volunteered to be the subject. The patients were recruited by the Feinberg School of Medicine at Northwestern University. There were no self-selection biases or other biases.

Magnetic resonance imaging

Experimental design

Design type	Event-related functional MRI
Design specifications	For the EMG task, the experiment consisted of 5 blocks of 18 trials each, for a total of 90 muscle contractions. Each contraction level was cued 6 times per block in a counterbalanced order, providing a total of 30 trials per contraction level. The contraction cues were presented for 2 seconds, and were followed by presentation of a fixation cross for 20 seconds during each inter-stimulus interval.
Behavioral performance measures	EMG amplitude induced by different levels of muscle contraction.

Acquisition

Imaging type(s)	Functional and structural MRI
Field strength	3 Tesla
Sequence & imaging parameters	EEG, ECG, and MRI acquisition: High-resolution structural information was obtained with a MPRAGE (Magnetization Prepared RApid Gradient Echo) structural scan, field of view (FOV): 230 mm x 230 mm, 256 x 256 matrix size, 0.9 mm slice thickness, 192 slices, repetition time (TR) = 2,000 ms, echo time (TE) = 2.32 ms, Inversion time (TI) = 900 ms, and GeneRalized Autocalibrating Partial Parallel Acquisition (GRAPPA) acceleration factor 2. Functional MRI data were collected with an Echo-Planar Imaging (EPI) scan, FOV: 240 mm x 240 mm, 92 x 92 matrix size, 4 mm slice thickness with 10% distant factor, 25 slices, TR = 2,000 ms, TE = 25 ms, and GRAPPA acceleration factor 2. We performed five scans, each consisting of 100 measurements, and flip angles of 10°, 30°, 50°, 70°, and 90°. For EMG and MRI acquisition: High-resolution structural information was obtained with a MPRAGE structural scan, FOV: 230 mm x 230 mm, 256 x 256 matrix size, 0.9 mm slice thickness, 192 slices, TR = 2,000 ms, TE = 2.32 ms, TI = 900 ms, and GRAPPA acceleration factor 2. Functional MRI data were collected with an EPI scan, FOV: 240 mm x 240 mm, 92 x 92 matrix size, 4 mm slice thickness with 10% distant factor, 25 slices, TR = 2,000 ms, TE = 30 ms, GRAPPA acceleration factor 2, and flip angle 90°.
Area of acquisition	A whole brain scan.

Diffusion MRI ☐ Used ☒ Not used

Preprocessing

Preprocessing software	Preprocessing of fMRI data was performed using SPM12 (Wellcome Department of Cognitive Neurology, London, UK), and analyses were performed using SPM12 and in-house MATLAB tools. For preprocessing, fMRI data were first corrected for differences in acquisition time between slices for each image. Second, each functional image was spatially realigned to the first image of each run to correct for head movement, and was co-registered to the participant's high-resolution 3D anatomical image. Third, these functional images were transformed into the standard anatomical space defined by the Montreal Neurological Institute (MNI) template implemented in SPM12. Finally, the normalized functional images were spatially smoothed using an 8 mm Gaussian kernel, full-width-at-half-maximum (FWHM), to increase the signal-to-noise ratio.
Normalization	Functional images were transformed into the standard anatomical space defined by the Montreal Neurological Institute (MNI) template implemented in SPM12 using the default segmentation-based normalization procedure.
Normalization template	The standard SPM12 template space defined by the Montreal Neurological Institute (MNI) was used.
Noise and artifact removal	Each functional image was spatially realigned to the first image of each run to correct for head movement using SPM12. Motion parameters confirmed that the participant did not have excessive motion (< +/-2.5 mm translation and < +/–1.5 degrees rotation over 5 task blocks).
Volume censoring	None

Statistical modeling & inference

Model type and settings	In-house custom MATLAB scripts involving whole-brain voxel-wise analyses were used to identify the TR/time point following trial onset, where the peak of blood-oxygen-level-dependent response occurred in expected brain regions such as the motor cortex. This examination was performed by selectively averaging the normalized smoothed functional brain images as a function of EMG trial type (that is, Small, Medium, Large) and time point (one pre-stimulus and 5 post-stimulus onset time points). No assumption was made about the shape of the haemodynamic response function because this method allows finer comparisons of the MR signal on a TR-by-TR basis. The analysis produced whole-brain average maps for each condition and TR/time point, which identified the time point covering 6–8 seconds post stimulus onset as the clearest peak of BOLD response in regions such as motor cortex for each condition. Thus, to identify coupling between variations in brain response and muscle contractions, fMRI-EMG associations were examined between the fMRI signals at this time point and EMG amplitude, on a trial-by-trial basis.
Effect(s) tested	The average EMG amplitude values in the duration of 1 s to 2 s were regressed onto the fMRI signals at each voxel in the brain for the time point following the onset of the trial that captures the peak of the BOLD response (6–8 seconds

post stimulus onset), on a trial-by-trial basis. The resulting statistical maps allowed for identification of associations between muscle response and brain activity related to the muscle contraction cues across trials.

Specify type of analysis: ☒ Whole brain ☐ ROI-based ☐ Both

Statistic type for inference (See Eklund et al. 2016)	A voxel-wise threshold of 4.94 t critical value, corresponding to $p < 0.05$, family-wise error (FWE) corrected for multiple comparisons, and an extent threshold of 100 voxels, was used for statistical testing.
Correction	A threshold of $p < 0.05$, family-wise error (FWE) corrected for multiple comparisons was used, implemented in SPM12 for whole brain analysis. An extent threshold of 100 voxels was used.

Models & analysis

n/a	Involved in the study
☒	☐ Functional and/or effective connectivity
☒	☐ Graph analysis
☒	☐ Multivariate modeling or predictive analysis

nature biomedical engineering

SUPPLEMENTARY INFORMATION
https://doi.org/10.1038/s41551-019-0347-x

In the format provided by the authors and unedited.

Large-area MRI-compatible epidermal electronic interfaces for prosthetic control and cognitive monitoring

Limei Tian[1,2,14], Benjamin Zimmerman[2,14], Aadeel Akhtar[2,14], Ki Jun Yu[3,14], Matthew Moore[2], Jian Wu[4], Ryan J. Larsen[2], Jung Woo Lee[5], Jinghua Li[6], Yuhao Liu[6], Brian Metzger[2], Subing Qu[6], Xiaogang Guo[4], Kyle E. Mathewson[7], Jonathan A. Fan[8], Jesse Cornman[9], Michael Fatina[9], Zhaoqian Xie[10], Yinji Ma[4], Jue Zhang[6], Yihui Zhang[4], Florin Dolcos[2], Monica Fabiani[2], Gabriele Gratton[2], Timothy Bretl[11], Levi J. Hargrove[12], Paul V. Braun[6], Yonggang Huang[10] and John A. Rogers[2,6,13]*

[1]Department of Biomedical Engineering, Texas A&M University, College Station, TX, USA. [2]Beckman Institute for Advanced Science and Technology, University of Illinois at Urbana–Champaign, Urbana, IL, USA. [3]School of Electrical and Electronic Engineering, Yonsei University, Seoul, Republic of Korea. [4]Applied Mechanics Laboratory, Department of Engineering Mechanics, Center for Mechanics and Materials and Center for Flexible Electronics Technology, Tsinghua University, Beijing, China. [5]Department of Materials Science and Engineering, Pusan National University, Busan, Republic of Korea. [6]Department of Materials Science and Engineering, Frederick Seitz Materials Research Laboratory, University of Illinois at Urbana–Champaign, Urbana, IL, USA. [7]Department of Psychology, University of Alberta, Edmonton, Alberta, Canada. [8]Department of Electrical Engineering, Stanford University, Stanford, CA, USA. [9]Department of Electrical and Computer Engineering, University of Illinois at Urbana–Champaign, Urbana, IL, USA. [10]Departments of Civil and Environmental Engineering, Mechanical Engineering, and Materials Science and Engineering, Northwestern University, Evanston, IL, USA. [11]Department of Aerospace Engineering, University of Illinois at Urbana–Champaign, Urbana, IL, USA. [12]Feinberg School of Medicine, Northwestern University, Shirley Ryan AbilityLab, Chicago, IL, USA. [13]Departments of Materials Science and Engineering, Biomedical Engineering, Neurological Surgery, Chemistry, Mechanical Engineering, Electrical Engineering and Computer Science, Simpson Querrey Institute and Feinberg Medical School Center for Bio-Integrated Electronics, Northwestern University, Evanston, IL, USA. [14]These authors contributed equally: Limei Tian, Benjamin Zimmerman, Aadeel Akhtar, Ki Jun Yu.
*e-mail: jrogers@northwestern.edu

Table of Contents

Figure S1. Comparison of flexible PCB and epidermal devices 2

Figure S2. Mechanics of an epidermal electrode mounted on the skin 3

Figure S3. SEM images of a bilayer soft support laminated on skin replica 4

Figure S4. Structure designs for electrodes with different fill factors 5

Figure S5. Equivalent circuit model of the electrode-skin-body interface 6

Table S1. Summary of fitted parameters using the equivalent circuit model 6

Figure S6. Conventional EMG systems and performance 7

Table S2. Comparison of confusion matrix with epidermal and conventional devices 8

Table S3. Property comparisons between conventional and epidermal EMG electrodes 9

Table S4. Comparison of confusion matrix with epidermal devices, before and after donning and doffing 10

EEG Recording with Emotion-Cognition Interactions Task 11

Figure S7. Scalp ERP maps measured in the emotion-cognition interaction task 12

Figure S8. Electromagnetic simulation model of electrodes in MRI 13

Figure S9. Calculations of magnetic field gradients with different electrode structures, including closed mesh, open mesh and conventional open ring in MRI 14

Figure S10. Calculations of magnetic field gradients with different open mesh designs in MRI 15

Figure S11. Calculations of electric fields with open mesh and conventional open ring electrodes under RF and under magnetic gradients 16

References 17

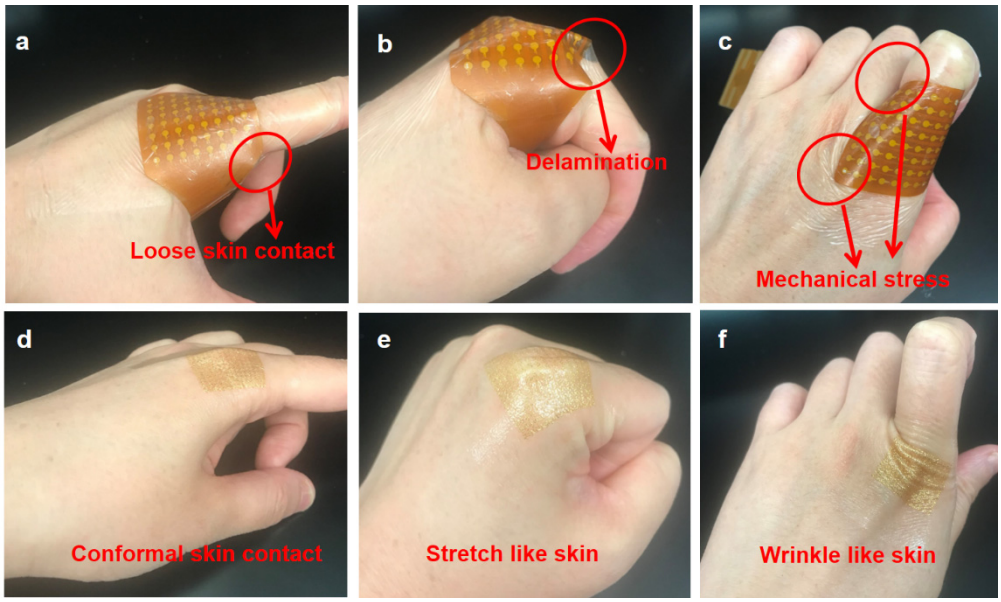

Figure S1. Comparison of flexible PCB (fPCB) and epidermal devices. (a-c) Photographs of a flexible PCB device interfaced to the skin under various states of deformation. (d-f) Photographs of an epidermal device interfaced to the skin under various states of deformation.

Figure S1 presents images that compare skin interfaces formed with fPCB and epidermal devices with similar overall thicknesses of 100 μm, lateral dimensions and electrode layouts, interfaced to the skin on a knuckle of the hand, under various states of deformation. The fPCB device loosely interfaces with the skin at the most strongly curved regions, even when mounted with 3M Tegaderm adhesive film (Figure S1a). The device is not stretchable, and therefore easily delaminates from the skin, and often induces irritation at the skin interface due to concentrated mechanical stress at certain regions (Figure S1b-c). In contrast, the epidermal device bends, stretches, and winkles without constraint on the natural motions of the skin (Figure S1d-f), thereby providing a robust, conformal electrical interface without motion-induced artifacts or irritation.

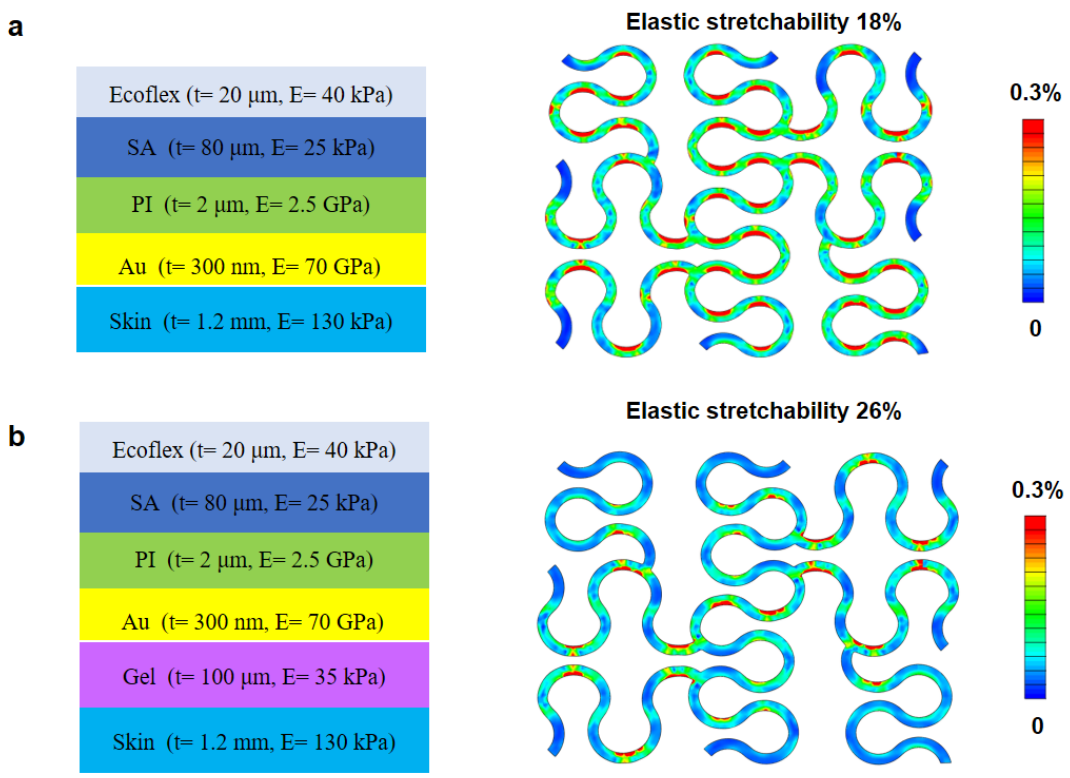

Figure S2. Mechanics of materials and structures for an epidermal electrode mounted on the skin. Cross-sectional illustration of representative layers in a stretchable electronic system without (a) and with conductive gel (b), and calculated distributions of principal strains in the metal upon uniaxial stretching to yield the elastic stretchability for each system.

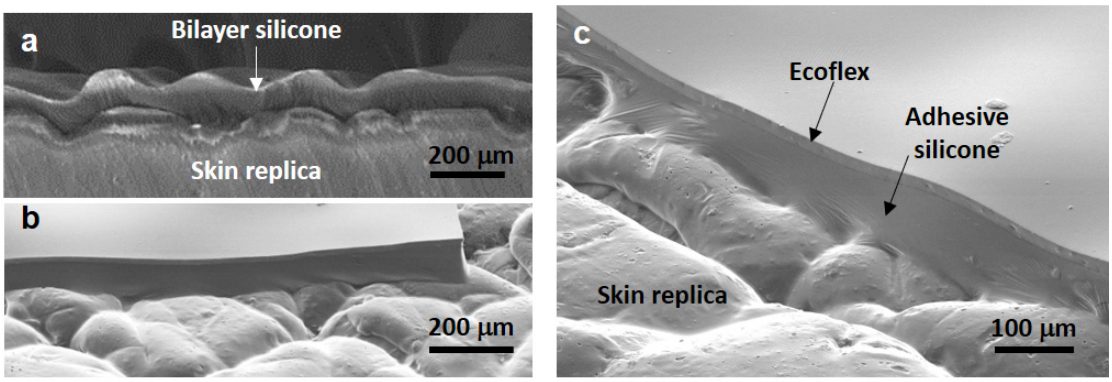

Figure S3. SEM images of a bilayer soft support laminated on a skin replica in cross section (a) and tilted views (b), (c).

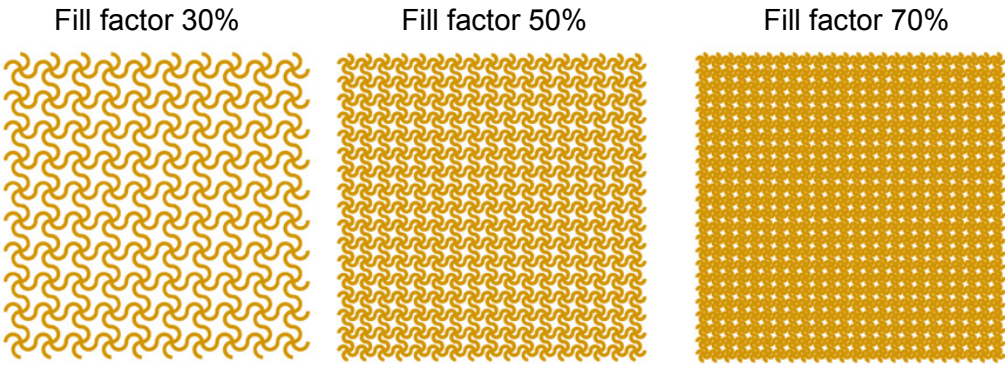

Figure S4. Structure designs of 1 cm x 1 cm electrodes with different fill factors including 30%, 50% and 70% (wire width 100 μm).

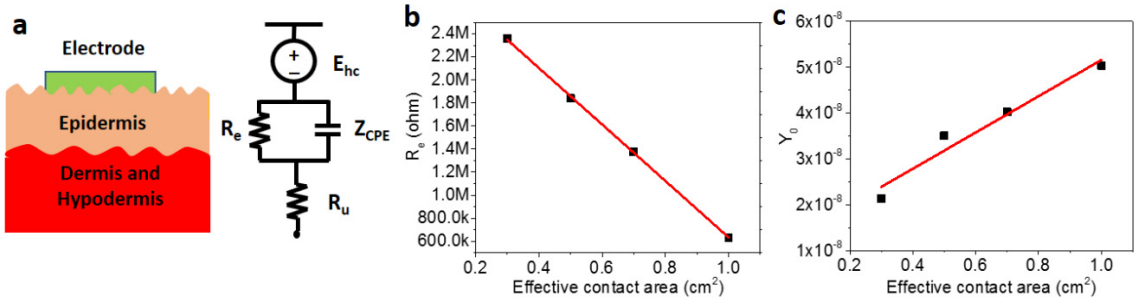

Figure S5. (a) Equivalent circuit model of the electrode-skin-body interface. (b) Fitted parameters R_e and Y_0, showing a linear decrease and increase with increasing effective contact area of electrodes on the skin, respectively.

Area (cm^2)	R_e (ohm)	R_u (ohm)	Y_0	alpha
1	6. 34E+05	3. 33E+02	5. 04E−08	0. 833033
0. 7	1. 38E+06	1. 72E+02	4. 02E−08	0. 848667
0. 5	1. 84E+06	1. 62E+02	3. 50E−08	0. 825933
0. 3	2. 36E+06	1. 81E+02	2. 14E−08	0. 814867

Table S1. Summary of fitted parameters using the equivalent circuit model.

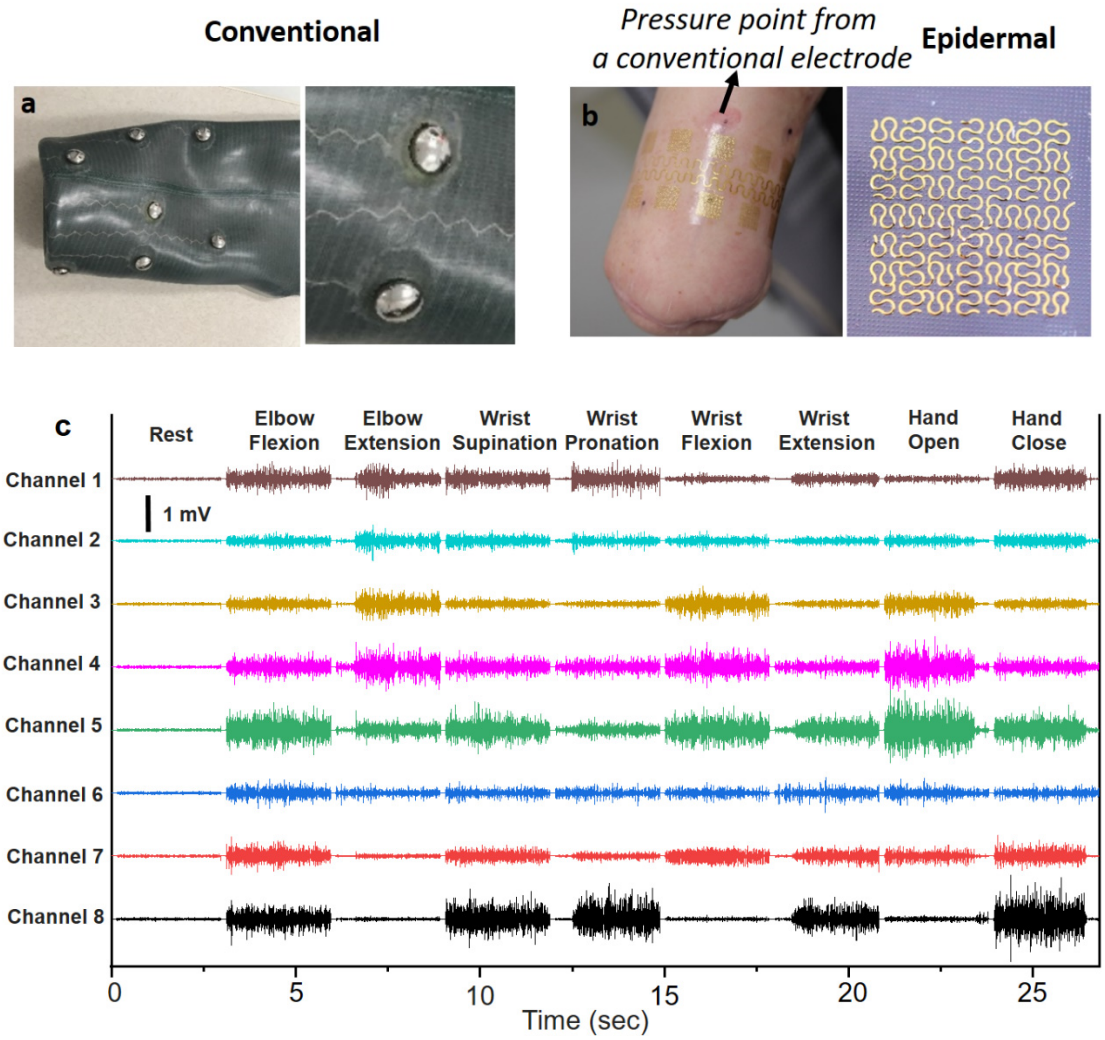

Figure S6. (a) Photographs of conventional EMG rigid electrodes embedded in a rubber prosthetic liner. (b) Photographs of an epidermal EMG array on the upper limb of a transhumeral amputee and an individual electrode on the microperforated soft support. (c) Multichannel EMG measured from the device shown in a.

Epidermal
Avg Accuracy 89%

Confusion Matrix (%)

<----Predicted---->

<----Actual---->

	No Movmt	Elb Flx	Elb Ext	Wrist Sup	Wrist Pro	Wrist Flx	Wrist Ext	Hand Open	Chuck Grip
No Movmt	100	0	0	0	0	0	0	0	0
Elb Flx	0	100	0	0	0	0	0	0	0
Elb Ext	0	0	99	0	0	0	0	0	0
Wrist Sup	1	0	0	69	2	15	0	0	13
Wrist Pro	0	0	1	0	97	1	0	0	0
Wrist Flx	0	0	2	0	0	91	0	0	6
Wrist Ext	0	0	17	0	0	0	82	0	0
Hand Open	1	0	0	0	0	0	3	96	0
Chuck Grip	0	0	0	18	0	19	0	0	62

Conventional
Avg Accuracy 84%

Confusion Matrix (%)

<----Predicted---->

<----Actual---->

	No Movmt	Elb Flx	Elb Ext	Wrist Sup	Wrist Pro	Wrist Flx	Wrist Ext	Hand Open	Chuck Grip
No Movmt	100	0	0	0	0	0	0	0	0
Elb Flx	2	79	0	2	0	0	11	0	5
Elb Ext	7	0	93	0	0	0	0	0	0
Wrist Sup	1	0	0	55	0	0	11	0	33
Wrist Pro	1	0	0	0	98	0	0	0	0
Wrist Flx	3	0	0	0	0	52	0	45	0
Wrist Ext	4	0	0	0	0	0	96	0	0
Hand Open	9	0	0	0	0	0	0	91	0
Chuck Grip	2	0	0	0	0	0	4	0	93

Table S2. Comparison of confusion matrix showing the average classification accuracy determined using EMG data collected with epidermal and conventional devices.

	Conventional	Epidermal
Materials type	Stainless steel	Gold/PI/silicone
Thickness	~2 mm	~300 nm/2 μm/100 μm
Weight	~1.3 g/cm^2	~10 mg/cm^2
Modulus	~200 GPa	~50 kPa
Bending stiffness	~150 N/m	~9x10^{-9} N/m
Thermal mass	650 mJ/cm^{2}K	14 mJ/cm^{2}K
Water vapor permeability	Depending on liner materials	WVTR 10 g/m^{2}h
Stretchablility of electrode	0%	~30%
Skin-electrode contact	Non-conformal	Conformal
Electro-myostimulation	Not suitable	Comfortable sensation

Table S3. Comparison of conventional and epidermal EMG electrodes.

Epidermal
Avg Accuracy 89%

After donning and doffing →

Epidermal
Avg Accuracy 87%

Confusion Matrix (%)

<----Predicted---->

Actual	No Movmt	Elb Flx	Elb Ext	Wrist Sup	Wrist Pro	Wrist Flx	Wrist Ext	Hand Open	Chuck Grip
No Movmt	100	0	0	0	0	0	0	0	0
Elb Flx	0	100	0	0	0	0	0	0	0
Elb Ext	0	0	99	0	0	0	0	0	0
Wrist Sup	1	0	0	69	2	15	0	0	13
Wrist Pro	0	0	1	0	97	1	0	0	0
Wrist Flx	0	0	2	0	0	91	0	0	6
Wrist Ext	0	0	17	0	0	0	82	0	0
Hand Open	1	0	0	0	0	0	3	96	0
Chuck Grip	0	0	0	18	0	19	0	0	62

Confusion Matrix (%)

<----Predicted---->

Actual	No Movmt	Elb Flx	Elb Ext	Wrist Sup	Wrist Pro	Wrist Flx	Wrist Ext	Hand Open	Chuck Grip
No Movmt	100	0	0	0	0	0	0	0	0
Elb Flx	1	69	0	0	0	7	0	0	23
Elb Ext	0	0	89	0	1	0	9	0	0
Wrist Sup	1	0	0	50	0	3	0	0	46
Wrist Pro	0	0	0	0	96	0	3	0	0
Wrist Flx	1	0	0	0	1	97	0	0	1
Wrist Ext	2	0	0	0	0	0	93	6	0
Hand Open	1	0	0	0	0	0	1	97	0
Chuck Grip	1	0	0	1	0	5	0	0	93

Table S4. Comparison of confusion matrix showing the average classification accuracy determined using EMG data collected with epidermal devices, before and after donning and doffing.

EEG Recording with Emotion-Cognition Interactions Task

The participant underwent recording of EEG while performing an emotional oddball task.[1] During the task, the participant detected "oddball" target stimuli (shapes) presented in a string of standard (scrambled) and distracter (emotional and neutral) stimuli. The oddball task consisted of 595 scrambled image trials, 60 target trials, 45 emotional (40 negative, 5 positive) distracter trials, and 40 neutral distracter trials, each of which were displayed for 1250 ms; a fixation cross was presented for 750 ms during the inter-stimulus intervals. The infrequent distracter stimuli (negative, positive, and neutral pictures) were selected from the International Affective Picture System (IAPS),[2] based on normative ratings for valence and arousal and were supplemented with in-house pictures used in previous studies.[1, 3] Positive distracters were included to provide a positive anchor in contrast to neutral and negative distracters, and to reduce the likelihood of inducing a negative mood by the unpleasant pictures. For the purposes of analyses, standards, neutral distracters, negative distracters, and targets were compared to assess differences in the associated brain activity (i.e., oddball targets vs. distracters and standards).

EEG Data Acquisition and Preprocessing

EEG data were acquired using an epidermal EEG electrode array and EOG electrodes with a Brain Products BrainAmp, at a sampling rate of 500 Hz. EOG electrodes were placed below the right eye, and at the outer canthi of the left and right eyes. Data were processed using EEGLAB [4] for down-sampling to 250 Hz, low-pass FIR filtering at 30 Hz, and high-pass FIR filtering at 0.1 Hz, followed by re-referencing to average mastoids. The EEG data were segmented time-locked to the onset of the stimulus, using a time window of -200 ms to 1250 ms. Trials in which EEG data exceeded ±70 μV in amplitude were rejected, to remove trials likely affected by eye movements or blinks.

EEG Results

As expected based on the extant literature[1], EEG data acquired during the emotional oddball showed large amplitude ERPs over posterior electrode locations for targets, within a time window of 250-450 ms. The topography and timing of this response is consistent with a P3 waveform (Figure S6). These results confirm that expected EEG signals can be successfully acquired using a large array of epidermal sensors.

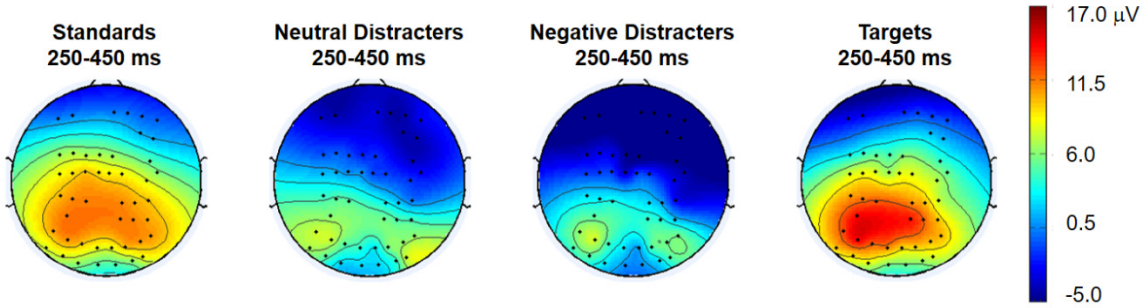

Figure S7. Scalp ERP maps showing the potential differences between standard, neutral distracter, negative distracter, and target conditions, measured in the emotion-cognition interaction task. The ERP was averaged within the time interval of 250-450 ms.

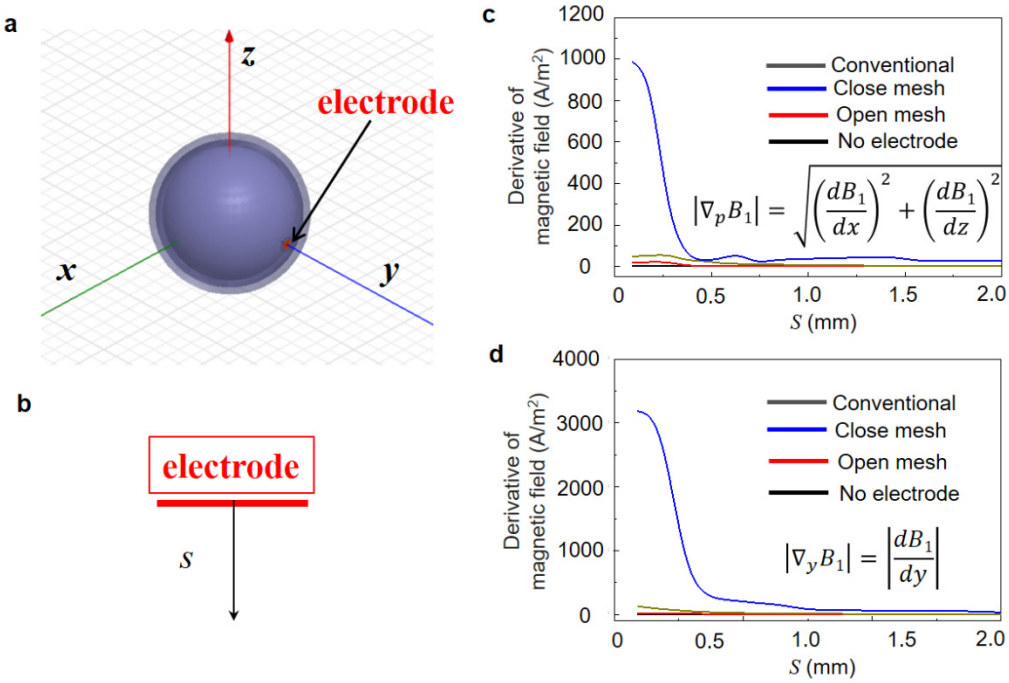

Figure S8. (a) Schematic illustration of an electromagnetic simulation model, composed of an electrode on the skin surface of a human head. (b) Cross-sectional illustration of the electrode on the scalp surface. Comparison of in-plane (c) and out-of-plane (d) derivatives of magnetic field in the head away from the electrodes for different structure designs.

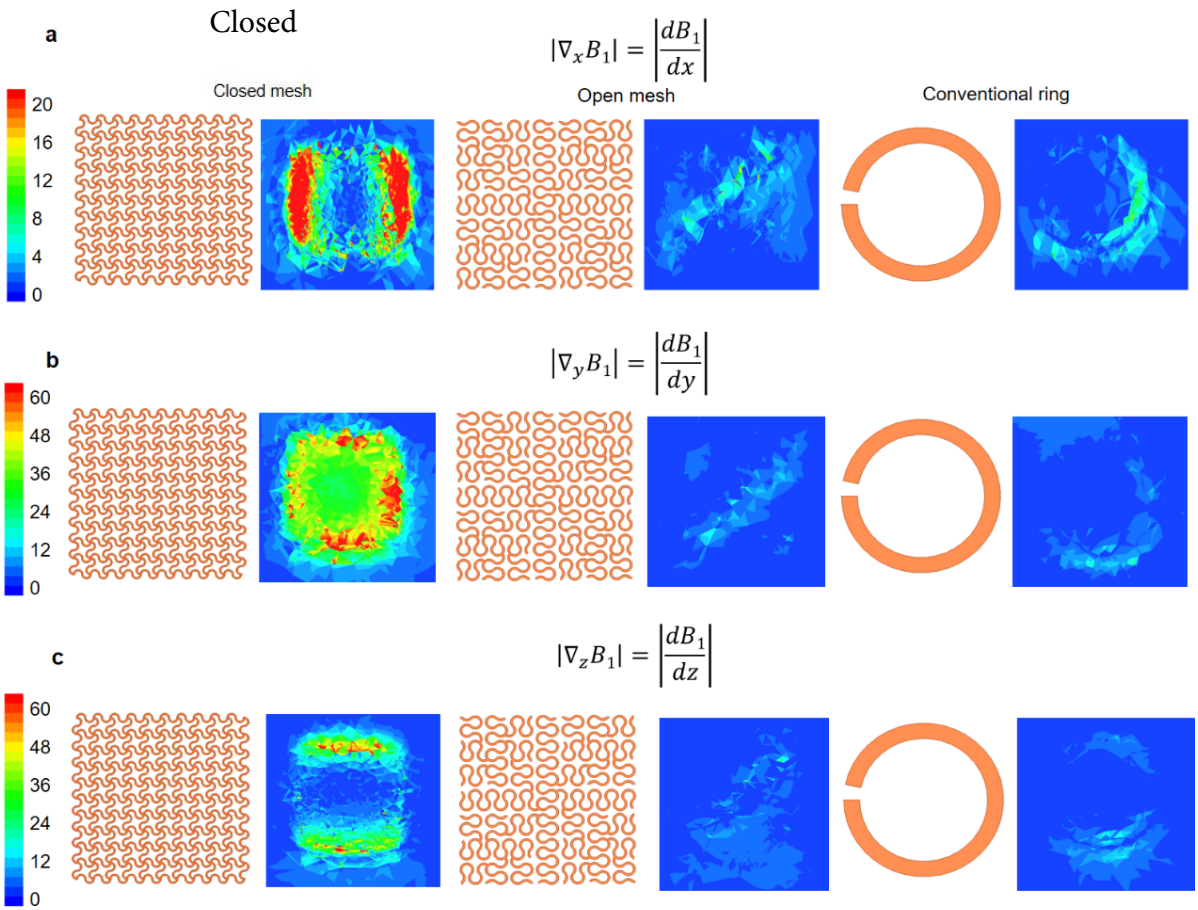

Figure S9. Calculations of the gradient of the magnetic field in the plane located 1 mm underneath electrodes with different structures, including closed mesh, open mesh and conventional open ring, along all the individual coordinate axes (a) $|\nabla_x B_1|$, (b) $|\nabla_y B_1|$, (c) $|\nabla_z B_1|$.

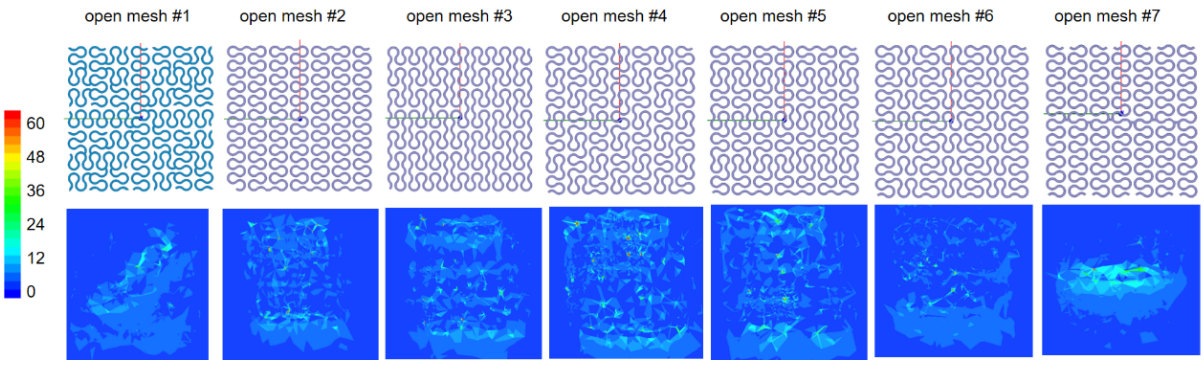

Figure S10. Calculations of the in-plane gradient of the magnetic field in the plane 1 mm underneath electrodes with different open mesh designs.

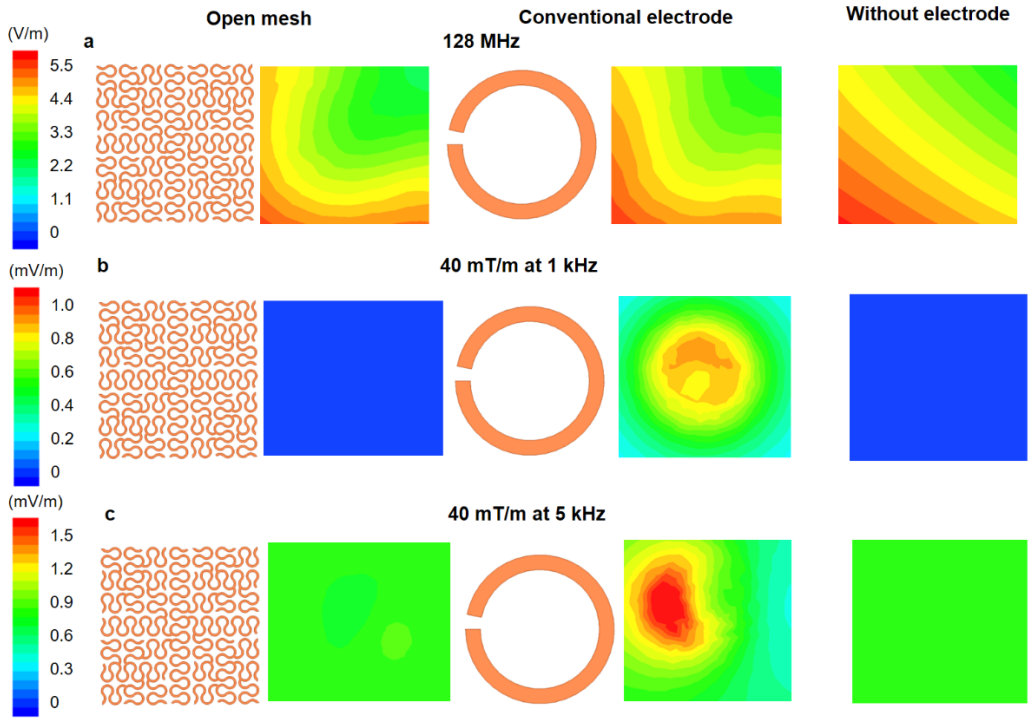

Figure S11. Calculations of the electric fields in a plane 5 mm underneath the electrode into the head induced by electrodes with open mesh and conventional open ring designs, compared to the case without the presence of an electrode, (a) under RF at 128 MHz, (b) under a magnetic gradient of 40 mT/m at 1 kHz, (c) under a magnetic gradient of 40 mT/m at 5 kHz.

References

1. Singhal, A.; Shafer, A. T.; Russell, M.; Gibson, B.; Wang, L.; Vohra, S.; Dolcos, F., Electrophysiological correlates of fearful and sad distraction on target processing in adolescents with attention deficit-hyperactivity symptoms and affective disorders. *Frontiers in Integrative Neuroscience* 2012, *6*, 119.

2. Lang, P. J.; Bradley, M. M.; Cuthbert, B. N., *International affective picture system (IAPS): Affective ratings of pictures and instruction manual. Technical Report A-8.* University of Florida, Gainesville, FL.: 2008.

3. Wang, L.; McCarthy, G.; Song, A. W.; Labar, K. S., Amygdala activation to sad pictures during high-field (4 tesla) functional magnetic resonance imaging. *Emotion* 2005, *5* (1), 12-22.

4. Delorme, A.; Makeig, S., EEGLAB: An open source toolbox for analysis of single-trial EEG dynamics including independent component analysis. *Journal of Neuroscience Methods* 2004, *134* (1), 9-21.